

FURTHER EVIDENCE FOR LARGE CENTRAL MASS-TO-LIGHT RATIOS IN EARLY-TYPE GALAXIES: THE CASE OF ELLIPTICALS AND LENTICULARS IN THE A262 CLUSTER*

G. A. WEGNER^{1,7}, E. M. CORSINI^{2,3}, J. THOMAS⁴, R. P. SAGLIA⁴, R. BENDER^{4,5}, AND S. B. PU⁶

¹ Department of Physics and Astronomy, 6127 Wilder Laboratory, Dartmouth College, Hanover, NH 03755-3528, USA

² Dipartimento di Fisica e Astronomia “G. Galilei,” Università di Padova, vicolo dell’Osservatorio 3, I-35122 Padova, Italy

³ INAF–Osservatorio Astronomico di Padova, vicolo dell’Osservatorio 2, I-35122 Padova, Italy

⁴ Max-Planck-Institut für extraterrestrische Physik, Giessenbachstraße, D-85748 Garching, Germany

⁵ Universitäts-Sternwarte München, Scheinerstraße 1, D-81679 München, Germany

⁶ The Beijing No. 12 High School, No. 15, YiZe Road, FengTai District, 100071 Beijing, China

Received 2012 February 7; accepted 2012 June 22; published 2012 August 6

ABSTRACT

We present new radially resolved spectroscopy of eight early-type galaxies in the A262 cluster. The measurements include stellar rotation, velocity dispersion, H_3 and H_4 coefficients of the line-of-sight velocity distribution along the major and minor axes and an intermediate axis as well as line-strength index profiles of Mg, Fe, and $H\beta$. The ionized-gas velocity and velocity dispersion is measured for six sample galaxies along different axes. We derive dynamical mass-to-light ratios and dark matter densities from orbit-based dynamical models, complemented by the galaxies’ ages, metallicities, and α -element abundances from single stellar-population models. The ionized-gas kinematics give a valuable consistency check for the model assumptions about orientation and intrinsic shape of the galaxies. Four galaxies have a significant detection of dark matter and their halos are about 10 times denser than in spirals of the same stellar mass. By calibrating dark matter densities to cosmological simulations we find assembly redshifts of $z_{\text{DM}} \approx 1-3$, as previously reported for the Coma Cluster. The dynamical mass that follows the light is larger than expected for a Kroupa stellar initial mass function (IMF), especially in galaxies with high velocity dispersion σ_{eff} inside the effective radius r_{eff} . This could indicate a “massive” IMF in massive galaxies. Alternatively, some of the dark matter in massive galaxies could follow the light very closely. In combination with our comparison sample of Coma early-type galaxies, we now have 5 of 24 galaxies where (1) mass follows light to $1-3 r_{\text{eff}}$, (2) the dynamical mass-to-light ratio of all the mass that follows the light is large ($\approx 8-10$ in the Kron-Cousins R band), and (3) the dark matter fraction is negligible to $1-3 r_{\text{eff}}$. Unless the IMF in these galaxies is particularly “massive” and somehow coupled to the dark matter content, there seems to be a significant degeneracy between luminous and dark matter in at least some early-type galaxies. The role of violent relaxation is briefly discussed.

Key words: galaxies: abundances – galaxies: elliptical and lenticular, cD – galaxies: formation – galaxies: kinematics and dynamics – galaxies: stellar content

Online-only material: color figures, extended figure, machine-readable and VO tables

1. INTRODUCTION

The distribution of dark matter surrounding elliptical galaxies as well as the dynamical structure of these systems is not generally known. While the dynamical structure contains information about the assembly mechanism of elliptical galaxies, the mass distribution can be used to constrain the assembly epoch. For example, the simple spherical collapse model predicts that the central dark matter density scales with $(1 + z_{\text{DM}})^3$, where z_{DM} is the assembly redshift of the halo. Numerical simulations likewise predict a close relationship between halo concentration and assembly epoch (Wechsler et al. 2002).

Dynamical modeling of stellar kinematics allows the reconstruction of both the orbital structure and the mass distribution in elliptical galaxies, and thus offers crucial information about when and how elliptical galaxies formed. In the past several years we have published a series of papers (Thomas et al. 2004, 2005b, 2007a, 2007b, 2009a, 2009b, 2011) studying the distribution of dark matter and the dynamical structure of the elliptical galaxies of the Coma Cluster. For the dynamical analysis we

employed a refined three-integral axisymmetric orbit superposition code to model the systems of stars in order to determine their mass compositions and orbital structures. For each trial potential on a grid systematically probing a mass component that follows the light (with mass-to-light ratio Υ_*) and different dark matter profiles, we determined an orbit superposition that best matched the kinematic data published by Mehlert et al. (2000), Wegner et al. (2002), and Corsini et al. (2008) with the additional requirement of maximizing the model’s entropy. The optimal entropy maximalization and fit to the data were calibrated using Monte Carlo simulations of observationally motivated galaxy models. These simulations revealed that from typical Coma data, the mass distribution can be reconstructed with an accuracy of $\approx 15\%$. The comparison with the masses derived through strong gravitational lensing for elliptical galaxies with similar velocity dispersion confirmed this result.

We compared Υ_* to the mass-to-light ratio Υ_{SSP} predicted by the best-fit single stellar population (SSP) models to the line-strength indices as in Mehlert et al. (2003). We found that at face value a Salpeter initial mass function (IMF; Salpeter 1955) gives, on average, the best agreement between Υ_* and Υ_{SSP} . However, several arguments favor a Kroupa IMF (Kroupa 2001) for the underlying true stellar mass distribution.

We derived dark matter densities for the Coma ellipticals that are, on average, at least 13 times higher than in spirals of the

* Based on data collected with the 2.4 m Hiltner Telescope.

⁷ Visiting Astronomer, MDM Observatory, Kitt Peak, AZ, operated by a consortium of Dartmouth College, the University of Michigan, Columbia University, The Ohio State University, and Ohio University.

same stellar mass, consistent with the findings of Gerhard et al. (2001) for round galaxies. We concluded that elliptical galaxy halos have assembled earlier, around $z_{\text{DM}} \approx 1\text{--}3$. This agrees with the predictions of the semi-analytic galaxy formation models of De Lucia et al. (2006), with simulated ellipticals in a Coma-like cluster environment. Halos form hierarchically—less massive halos first. In contrast, studies on the star formation histories based on line indices (Nelán et al. 2005; Thomas et al. 2005a) show that stars form anti-hierarchically—the least massive galaxies have the youngest stellar populations. This would result from star formation following the hierarchical mass assembly to the time that the available gas is consumed or expelled; early star formation would occur in low-mass systems that subsequently merge, forming massive systems, and today, low-mass galaxies are generally late-assembling galaxies with younger stellar populations. We found that in a third of our Coma galaxies star formation and halo assembly redshifts match. The youngest galaxies must have experienced some star formation after the main halo assembly epoch—in line with their orbital structure being inconsistent with collisionless N -body mergers with no star formation of disk galaxies (Thomas et al. 2009a).

The Coma Cluster represents a high-density local cluster sample. In lower-density local environments, the stellar populations of ellipticals are formed at $z_* \leq 1$ (Wegner & Grogin 2008) and have a greater spread of ages—the oldest are about as old as cluster ellipticals, but the youngest are much younger (Collobert et al. 2006). Dark matter densities of ellipticals in the Coma Cluster are predicted to be lower because they assemble later. These predictions need now to be verified by models of real galaxies.

Here we present the new data set we collected for a sample of early-type galaxies of the nearby poor cluster A262. The results of the dynamical analysis we performed are compared to the Coma Cluster case. A262 is one of the most conspicuous condensations in the Pisces–Perseus supercluster. The center of the cluster coincides with the position of the cD galaxy NGC 708. A262 is far less densely populated than the Coma Cluster and is comparable to the Virgo Cluster. Indeed, it falls into richness class 0 (Abell et al. 1989). The cluster redshift of $z = 0.0163$ (Struble & Rood 1999) results in a distance of 70 Mpc, assuming $H_0 = 70 \text{ km s}^{-1} \text{ Mpc}^{-1}$. At this redshift the angular distance $1''$ corresponds to 339 pc. The cluster mass within the virial radius ($R_{\text{vir}} = 1.52$ corresponding to 1.9 Mpc) and calculated from the line-of-sight velocity dispersion of the cluster galaxies ($\sigma = 548 \pm 35 \text{ km s}^{-1}$) is $M_{\text{vir}} = (2.5 \pm 0.5) \times 10^{14} M_{\odot}$. It is in agreement with the mass estimated from X-ray data assuming hydrostatic equilibrium (Neill et al. 2001). The low X-ray luminosity (David et al. 1993), low temperature of the hot intracluster medium (Sato et al. 2009) with complex structure (Clarke et al. 2009), and a central cooling flow (Blanton et al. 2004) are typical signatures of a less evolved, dynamically young cluster.

The structure of the paper is as follows. In Section 2 we present the galaxy sample. We discuss the observations, data reduction, and analysis of the imaging data set in Section 3 and of the spectroscopic data set and the SSP analysis of the line-strength indices in Section 4. A summary of the dynamical modeling technique is given in Section 5 and a comparison with the gas kinematics and strong gravitational lensing masses follows in Section 6. The results are presented in Section 7 and their implications are discussed in Section 8. A summary of the paper follows in Section 9.

2. GALAXY SAMPLE

All the sample galaxies in A262 were studied within the EFAR (Ellipticals FAR away) project. The EFAR project was aimed at constructing an accurate and homogeneous photometric and spectroscopic database for a large sample of early-type galaxies at redshifts between 6000 and 15,000 km s^{-1} and distributed in 85 clusters in the Hercules–Corona Borealis and Perseus–Pisces–Cetus regions. Details about the selection of the EFAR galaxy and cluster sample are given by Wegner et al. (1996). Saglia et al. (1997b) and Wegner et al. (1999) presented the photometric and spectroscopic databases, respectively. Results from the project addressed the galaxy structural parameters (Saglia et al. 1997a), the properties of the stellar populations (Colless et al. 1999), the fundamental plane, peculiar velocities, and bulk motions (Saglia et al. 2001; Colless et al. 2001).

The galaxies studied here were selected to be round and were classified as early-type (cD, E, and E/S0) in Wegner et al. (1996). Their basic properties, which include morphological type, structural parameters, total magnitude, velocity dispersion, and redshift, can be found in Table 1.

3. OBSERVATIONS, DATA REDUCTION, AND ANALYSIS: IMAGING

3.1. Observations and Data Reduction

As part of the HST Snapshot Proposal 10884 (P.I.: G. A. Wegner), the galaxies NGC 679, NGC 687, NGC 708, NGC 759, and UGC 1308, were observed with the Wide Field Planetary Camera 2 (WFPC2) on board the *Hubble Space Telescope* (HST) between 2007 July 14 and 2008 September 27. For each galaxy, two 300 s exposures were taken with the filter F622W. All exposures were performed with the telescope guiding in fine lock, which typically gave an rms tracking error of $0''.003$. The centers of the galaxies were positioned on the Planetary Camera (PC) chip in order to get the best possible spatial resolution. This consists of 800×800 pixels of $0''.0455 \times 0''.0455$ each, yielding a field of view of about $36'' \times 36''$. The two pointings were shifted along the pixel diagonal by $0''.3535$. This pattern corresponds to a shift of 5.5×5.5 pixels on the PC chip.

In the following, our photometric analysis is limited to the PC chip since the nuclear surface-brightness profiles were matched to available radially extended ground-based photometry. Indeed, all the sample galaxies were observed in the R band of the Kron-Cousins system as a part of the EFAR project (Colless et al. 1993; Saglia et al. 1997b).

The WFPC2 images were reduced using the CalWFPC reduction pipeline in IRAF⁸ maintained by the Space Telescope Science Institute. Reduction steps include bias subtraction, dark current subtraction, and flat-fielding, as described in detail in the WFPC2 instrument and data handbooks (Baggett & McMaster 2002; McMaster & Biretta 2008). Subsequent analysis was performed using IRAF standard tasks. The bad pixels were corrected by means of a linear one-dimensional interpolation using the data quality files and the WFIXUP task. For each galaxy, the alignment of the images was checked by comparing the centroids of stars in the field of view. The images were aligned to an accuracy of a few hundredths of a pixel using IMSHIFT and knowledge of the offsets. They were then

⁸ The Imaging Reduction and Analysis Facility (IRAF) is distributed by the National Optical Astronomy Observatory, which is operated by the Association of Universities for Research in Astronomy (AURA), Inc., under cooperative agreement with the National Science Foundation.

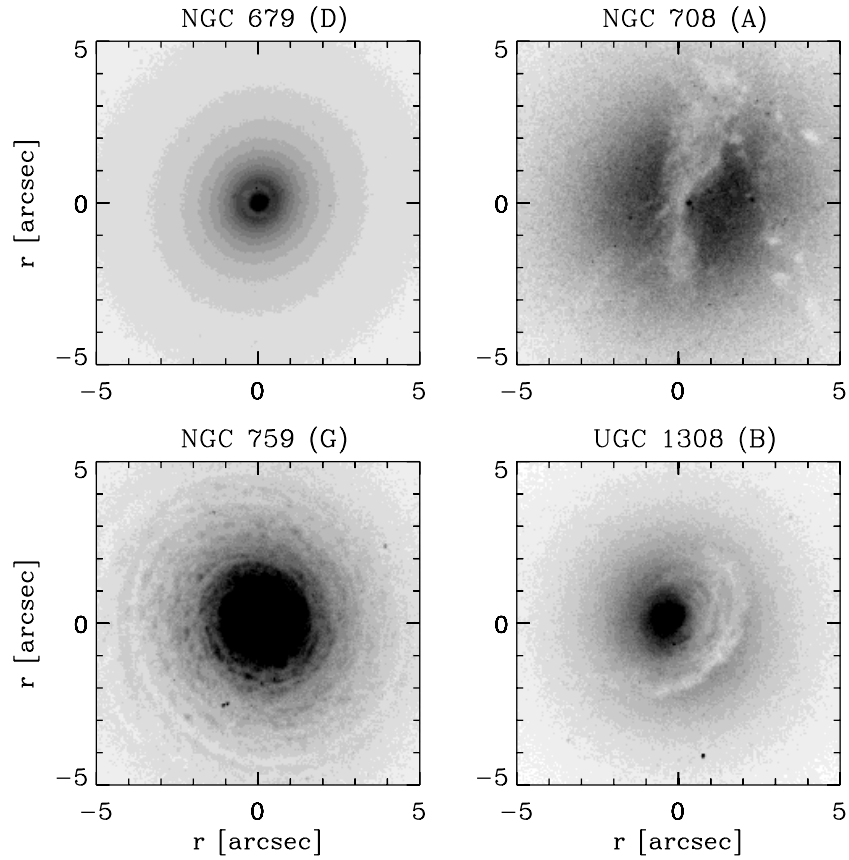


Figure 1. Central portions of *HST* WFPC2/F622W images of the galaxies showing dust features. Each frame uses a negative intensity scale and north is at the top with east to the left.

Table 1
Properties of the Sample Galaxies

Object	Alt. Name	Type	r_{eff} (arcsec)	$\langle\mu\rangle_{\text{eff}}$ (mag arcsec $^{-1}$)	R_{T} (mag)	P.A. ($^{\circ}$)	cz (km s $^{-1}$)	σ (km s $^{-1}$)	d (Mpc)
(1)	(2)	(3)	(4)	(5)	(6)	(7)	(8)	(9)	(10)
IC 171	A262 E	E	30.31	20.47	11.16	108	5346	178	1.22
NGC 679	A262 D	E	10.37	18.80	11.79	85	5036	229	0.88
NGC 687	A262 C	E/S0	12.79	19.19	11.74	...	5086	224	0.61
NGC 703	A262 I	E/S0	9.41	19.45	12.65	47	5584	180	0.04
NGC 708	A262 A	cD	33.03	21.00	11.48	39	4845	194	0
NGC 712	A262 F	E/S0	10.31	19.18	12.19	83	5330	221	0.82
NGC 759	A262 G	E/S0	16.24	19.72	11.74	...	4644	241	1.27
UGC 1308	A262 B	E	23.88	19.44	10.63	140	5227	216	0.50

Notes. Column 1: Name. Column 2: Alternative name from Wegner et al. (1996). Column 3: Morphological type from Wegner et al. (1996). In spite of the cD classification, the properties of NGC 708 are not particularly extreme with respect to the other A262 galaxies listed here. Column 4: Effective radius obtained by Saglia et al. (1997b) in the Kron-Cousins R band. Column 5: Average surface brightness within the effective radius obtained by Saglia et al. (1997b) in the Kron-Cousins R band after applying the Galactic absorption, K_R , and cosmological dimming corrections. Column 6: Total magnitude measured by Saglia et al. (1997b) in the Kron-Cousins R band after applying the Galactic absorption and K_R corrections. Column 7: Major-axis position angle measured north through east from the HyperLeda catalog (Paturel et al. 2003). Column 8: Heliocentric systemic velocity from Wegner et al. (1999). Column 9: Velocity dispersion measured by Wegner et al. (1999) after applying the correction to the standard metric aperture of $0.54 h^{-1}$ kpc in radius. Column 10: Projected distance from NGC 708.

combined with IMCOMBINE. A check was performed to verify that the alignment and combination did not introduce a significant blurring of the data. To this aim, the FWHM of the Gaussian fitting to the field stars was measured in the original and combined frames. It was found that they did not change to within a few percent. In combining the images, pixels deviating

by more than three times the local standard deviation (calculated from the combined effect of Poisson and readout noise) were flagged as cosmic rays and rejected. The residual cosmic rays and bad pixels were corrected by manually editing the resulting image with IMEDIT. The *HST* images of four of the galaxies are shown in Figure 1.

3.2. Isophotal Analysis

The reduced EFAR images were available to one of us (R.P.S.). To calibrate the images, the photometric zero points in Saglia et al. (1997b) were adopted and their coefficients were applied to correct the measured magnitudes for Galactic absorption and K_R correction and to correct the measured surface brightnesses for Galactic absorption, K_R correction, and cosmological dimming. The EFAR images were used to determine the zero points and calibrate the WFPC2 images.

To this aim, the isophotal profiles of the galaxies were measured by fitting the isophotes in the WFPC2 and EFAR images with ellipses using the isophotal shape algorithm described by Bender & Moellenhoff (1987). For the fitted isophotes the algorithm provides the azimuthally averaged surface brightness (μ), ellipticity (ϵ), position angle (P.A.), center coordinates (x_0 , y_0) and third, fourth, and sixth cosine (a_3 , a_4 , and a_6) and sine (b_3 , b_4 , and b_6) Fourier coefficients describing the deviation of the isophotal shape from a perfect ellipse. Foreground stars, residual cosmic rays, and bad pixels were masked before fitting. Moreover, the centers of ellipses were allowed to vary. As a first step, the sky background was measured in regions free of sources at the edges of the field of view and then subtracted. Its final value in the WFPC2 images was determined through the matching of the ground-based photometry.

The surface-brightness radial profiles measured in the WFPC2 images were matched to the EFAR ones typically between $3''$ and $10''$ by determining the zero point and sky value that minimize the surface-brightness flux differences. The galaxies were assumed to have no $R - m_{F622W}$ color gradient in the matched radial region. The resulting distribution of the differences $\Delta m = R - m_{F622W}$ after minimization gives a standard deviation about the mean $\sigma_{\Delta m} = 0.035$ mag for NGC 679, $\sigma_{\Delta m} = 0.017$ mag for NGC 687, and $\sigma_{\Delta m} = 0.050$ mag for UGC 1308. Therefore, the scatter $\sigma_{\Delta m}$ is the dominant source of error in the zero point of the WFPC2 images because the EFAR final data set has a common zero point to better than 0.01 mag (Saglia et al. 1997b).

The prominent dust lanes crossing the nucleus of NGC 708 (Figure 1) did not allow us to measure reliable isophotal parameters within a few arcseconds from the galaxy center in both the WFPC2 and EFAR images. To minimize the impact of dust on the measurement of the isophote shape, we analyzed the H -band image obtained by Gavazzi et al. (1996) retrieved from the GOLDMine Archive (Gavazzi et al. 2003). The near-infrared data were taken on 1995 February 13 at Calar Alto Observatory, Spain using the 2.2 m telescope mounted on the Max-Planck-Institut für Astronomie General-purpose Infrared Camera with a Rockwell 256×256 NICMOS3 HgCdTe detector array. The spatial scale was $1''.61 \text{ pixel}^{-1}$, yielding a field of view of $6''.8 \times 6''.8$. The total exposure time was 192 s. A two-dimensional fit with a circular Gaussian to the field stars in the resulting image yielded an FWHM = $2''.2$. The surface-brightness radial profiles measured in the GOLDMine and EFAR images were matched between $5''$ and $26''$ with $\langle \Delta m \rangle = +0.006$ mag and $\sigma_{\Delta m} = 0.026$ mag.

For NGC 679, NGC 687, NGC 759, and UGC 1308, the P.A.s measured in the available HST and ground-based available images match within 2° , ellipticities match within less than 0.05, cosine and sine Fourier coefficients match within less than 1%, and the center coordinates of the fitting ellipses match within $0''.2$.

The radial profiles of the azimuthally averaged surface brightness; ellipticity; P.A.; center coordinates; and third, fourth, and sixth cosine and sine Fourier coefficients of the sample galaxies are presented in Figure 2 and Table 5. For NGC 679, NGC 687, NGC 759, and UGC 1308 they are the combination of HST and EFAR data. For NGC 708 they are measured on the GOLDMine image. For IC 171, NGC 703, and NGC 712 they are obtained from the EFAR images.

3.3. Morphologies of the Galaxies with Dust

Classed as early-type galaxies on ground-based data (Wegner et al. 1996, but see also de Vaucouleurs et al. 1991), the HST images show that four of the galaxies in this investigation—NGC 679, NGC 708, UGC 1308, and NGC 759—have absorbing material in their central regions, as shown in Figure 1. These resemble the dust features described elsewhere (e.g., Martini et al. 2003; Lauer et al. 2005) and found in two of our Coma Cluster galaxies (Corsini et al. 2008). Only NGC 687 shows no dust features in its nucleus.

NGC 679. The nucleus of the galaxy hosts a nearly face-on ring of dust. It has a radius of $4''.5$ (1.5 kpc).

NGC 708. The strong dark stripe of NGC 708 appears to be consistent with a dust disk seen nearly edge-on as it runs roughly north–south through the center of the galaxy image. It extends out to $3''.2$ (1.1 kpc) on its south side and $5''.8$ (2.0 kpc) on the north side. Individual dark blobs can be seen along the edge of the band, particularly to the west side.

NGC 759. The galaxy has a nuclear dusty disk which is close to being face-on. It has a radius of $5''.0$ (1.7 kpc) and it is characterized by tightly wound multiple spiral arms.

UGC 1308. The galaxy nucleus appears to have an inclined dust disk. The projected elliptical shape has a major axis of $3''.2$ (1.1 kpc) across in the north–south direction and a minor axis of $2''.6$ (0.9 kpc). It is asymmetric in that it is stronger on the west side and is not present on the east side.

4. OBSERVATIONS, DATA REDUCTION, AND ANALYSIS: SPECTROSCOPY

4.1. Observations and Data Reduction

Long-slit spectroscopic data of the sample galaxies were obtained with the 2.4 m Hiltner telescope of the MDM Observatory at Kitt Peak, AZ on 2003 November 14–23 (run 1), 2005 October 25–31 (run 2), and 2006 November 10–16 (run 3).

In runs 1 and 2 the telescope mounted on the Moderate Resolution Spectrograph with a plane reflection grating with $1200 \text{ grooves mm}^{-1}$ blazed at 5000 \AA at the first order and a $1''.9 \times 9''.6$ slit. The “Echelle” CCD was adopted as detector. It is a thinned and backside-illuminated Site CCD with 2048×2048 pixels of $24 \times 24 \text{ \mu m}^2$. The gain and readout noise are $2.7 e^- \text{ ADU}^{-1}$ and $7.9 e^-$ (rms), respectively. In run 3 the Boller & Chivens CCD Spectrograph was mounted with a plane reflection grating with $600 \text{ grooves mm}^{-1}$ blazed at 5875 \AA in the second order. A $1''.7 \times 5''.2$ slit with an LG370 order-blocking filter was used. The “Ohio State University Loral C” CCD was the detector. The latter is a thinned and backside-illuminated Loral CCD with 1200×800 pixels of $15 \times 15 \text{ \mu m}^2$. The gain and readout noise are $2.1 e^- \text{ ADU}^{-1}$ and $7.0 e^-$ (rms), respectively. No pixel binning was adopted. The wavelength range from 4670 to 6541 \AA was covered with a reciprocal dispersion of $0.870 \text{ \AA pixel}^{-1}$ in run 1, from 4675 to 6530 \AA with $0.906 \text{ \AA pixel}^{-1}$ in run 2, and from 6270 to 7175 \AA with

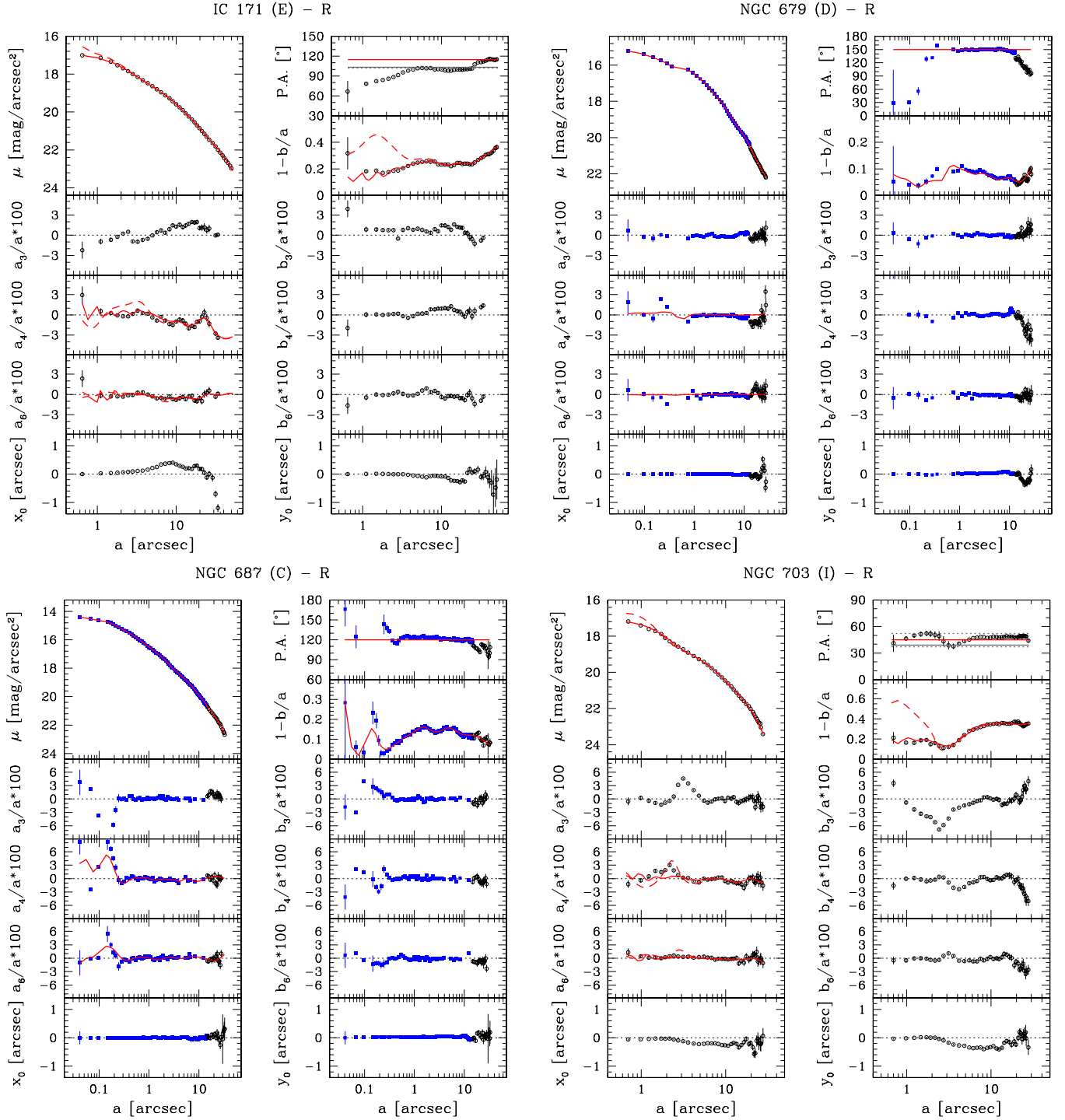


Figure 2. Isophotal parameters of the galaxies from ground-based (black open circles) and *HST*/WFPC2 images (blue filled squares) as a function of the logarithm of the semimajor-axis distance in arcseconds. The radial profiles of Kron-Cousins *R*-band surface brightness (μ); third, fourth, and sixth cosine Fourier coefficients (a_3 , a_4 , and a_6); and x -coordinate of the center (x_0) are plotted in the left panels (from top to bottom). The radial profiles of position angle (P.A.); ellipticity ($1 - b/a$); third, fourth, and sixth sine Fourier coefficients (b_3 , b_4 , and b_6); and y -coordinate of the center (y_0) are plotted in the right panels (from top to bottom). For galaxies with only ground-based photometry, the solid and dashed red lines correspond to the surface brightness, ellipticity, a_4 , and a_6 profiles obtained by projecting the deprojected stellar luminosity density with and without the correction for seeing convolution, respectively. For the remaining galaxies, the solid red lines are obtained by projecting the stellar luminosity density without the correction for seeing convolution. The solid gray line corresponds to the galaxy position angle (P.A._{gas}) derived by minimizing the difference between the rotation velocity of the ionized gas and the circular velocity from the dynamical model (see Section 6.2 for details). The gray dotted lines delimit the 68% confidence region for P.A._{gas}.

(A color version of this figure is available in the online journal.)

$0.755 \text{ \AA pixel}^{-1}$ in run 3. The spatial scale was $0''.606 \text{ pixel}^{-1}$ in runs 1 and 2, and $0''.41 \text{ pixel}^{-1}$ in run 3.

In runs 1 and 2 the spectra were obtained along the major, minor, and a diagonal axis for all the sample galaxies, except

for UGC 1308 which was observed only along the major and minor axis. The major axis of IC 171 and NGC 679 and the minor axis of UGC 1308 were observed in both runs to perform a consistency check between the measurements of

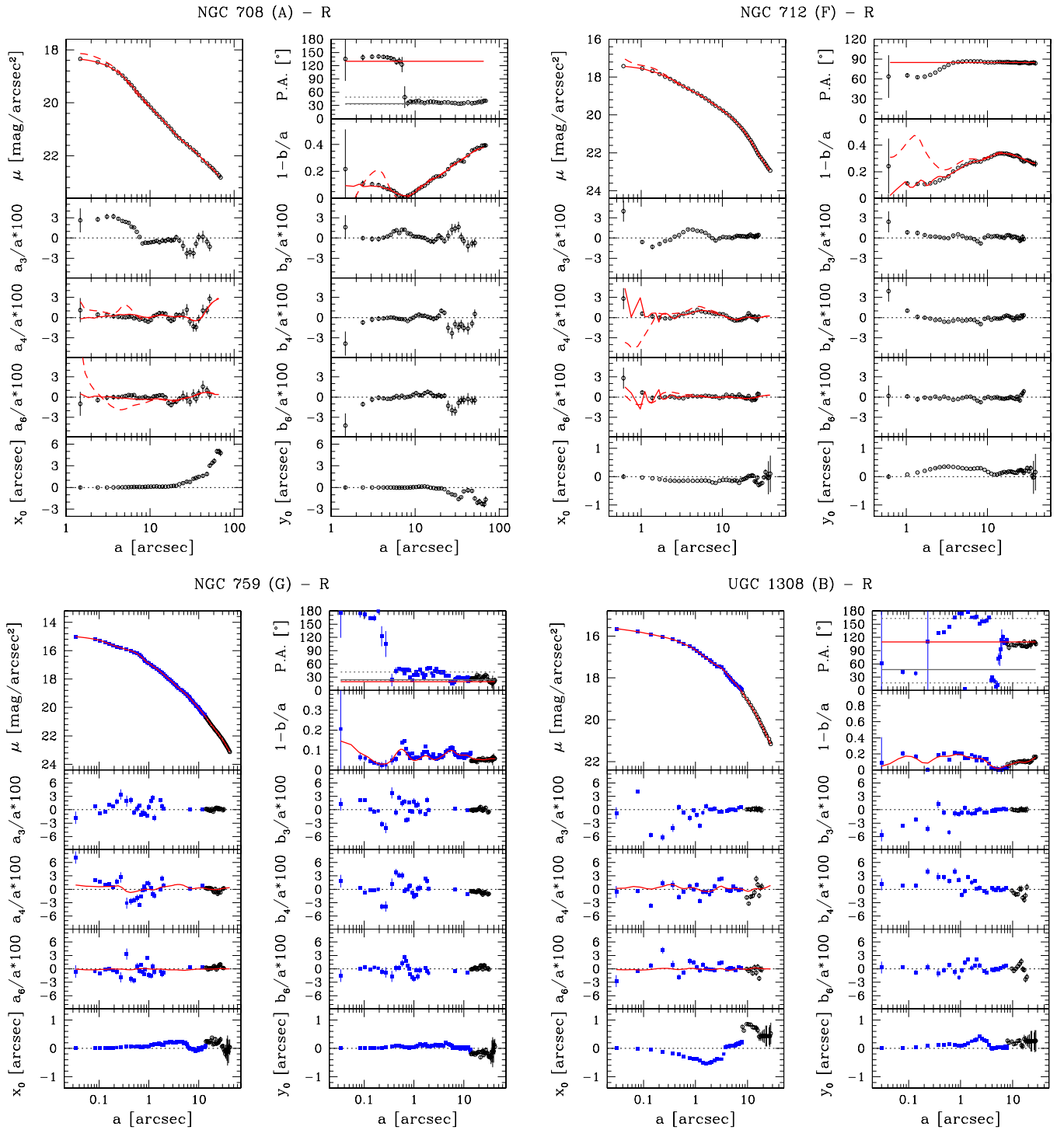


Figure 2. (Continued)

stellar kinematics and line-strength indices of the two runs. In run 3 the spectra were obtained along a diagonal axis. Only NGC 708 was also observed along the major and minor axes. For NGC 759 the spectra were also taken close to the major axis and along the minor axis. The integration time of the single galaxy spectra was 3600 s in runs 1 and 2 and 1800 s in run 3. Total integration times and slit P.A. of the galaxy spectra as well as the log of the spectroscopic observations are given in Table 2.

At the beginning of each exposure the galaxy was centered on the slit using the guiding camera which looks onto the slit. In runs 1 and 2 several spectra of giant stars with spectral type

ranging from late-G to early-K were obtained for templates in measuring stellar kinematics and line-strength indices. The template stars were selected from Faber et al. (1985) and González (1993). At least one flux standard star per night was observed to calibrate the flux of the spectra before line-strength indices were measured. Spectra of the comparison arc lamp were taken before and/or after object exposures.

All the spectra were bias-subtracted, flat-field corrected, cleaned of cosmic rays, corrected for bad columns, and wavelength and flux calibrated using standard IRAF routines. Each spectrum was rebinned using the wavelength solution obtained

Table 2
Log of the Spectroscopic Observations

Object	Run	P.A. ($^{\circ}$)	Position	Single Exp. Time (s)	Total Exp. Time (h)	Q
(1)	(2)	(3)	(4)	(5)	(6)	(7)
IC 171 (E)	3	0	DG	3×1800	1.5	4
	2	10	DG	3×3600	3.0	2
	1	110	MJ	4×3600	4.0	2
	2	110	MJ	1×3600	1.0	2
	2	145	DG	3×3600	3.0	2
NGC 679 (D)	1	0	DG	3×3600	3.0	1
	2	0	DG	1×3600	1.0	1
	3	0	DG	2×1800	1.0	4
	2	90	DG	3×3600	3.0	2
	2	135	MJ	4×3600	4.0	2
NGC 687 (C)	1	0	DG	3×3600	3.0	1
	3	0	DG	2×1800	1.0	4
	2	20	MN	3×3600	3.0	1
NGC 703 (I)	2	110	MJ	3×3600	3.0	1
	2	0	DG	3×3600	3.0	2
	3	0	DG	2×1800	1.0	4
NGC 708 (A)	1	45	MJ	3×3600	3.0	1
	2	135	MN	4×3600	4.0	2
	1	0	DG	1×3600	1.0	3
	3	0	DG	3×1800	1.5	3
	2	40	MN	3×3600	3.0	3
NGC 712 (F)	3	40	MN	3×1800	1.5	4
	2	130	MJ	3×3600	3.0	2
	3	130	MJ	3×1800	1.5	4
	3	0	DG	3×1800	1.5	4
	1	95	MJ	3×3600	3.0	2
NGC 759 (G)	2	125	DG	3×3600	3.0	2
	2	170	MN	4×3600	4.0	2
	3	0	DG	3×1800	1.5	4
	1	11	MJ	3×3600	3.0	1
UGC 1308 (B)	2	100	MN	3×3600	3.0	2
	3	100	MN	3×1800	1.5	4
	2	145	DG	3×3600	3.0	2
	3	145	DG	3×1800	1.5	4
	3	0	DG	2×1800	1.5	4
UGC 1308 (B)	1	28	MN	3×3600	3.0	2
	2	28	MN	2×3600	2.0	3
	2	120	MJ	3×3600	3.0	2

Notes. Column 1: Name. Column 2: Observing run. Column 3: Slit position angle measured north through east. Column 4: Slit position. MJ = major axis (or close to the major axis), MN = minor axis (or close to the minor axis), DG = diagonal axis. Column 5: Number and exposure time of the single exposures. Column 6: Total exposure time. Column 7: Estimated quality of the resulting spectrum. 1: excellent; 2: very good; 3: good; 4: fair (see Figure 3).

from the corresponding arc-lamp spectrum. The difference between the measured and predicted wavelengths in the comparison arc-lamp spectra have an rms of 0.05 \AA , corresponding to 3 km s^{-1} at 5170 \AA (i.e., the wavelength of the Mg I absorption triplet) in runs 1 and 2 and 2 km s^{-1} at $H\alpha$ in run 3. Systematic errors of the absolute wavelength calibration ($\leq 10 \text{ km s}^{-1}$) were estimated from the brightest night-sky emission lines in the observed spectral range (Osterbrock et al. 1996). The instrumental resolution in each run was derived as the mean of the Gaussian FWHMs measured for a number of unblended arc-lamp lines which were distributed over the whole spectral range of a wavelength-calibrated spectrum. The mean FWHM of the arc-lamp lines was 2.3 \AA in run 1 and 2.4 \AA in run 2 and the corresponding instrumental resolution was derived at 5170 \AA is $\sigma_{\text{inst}} \simeq 60 \text{ km s}^{-1}$. In run 3 the mean FWHM was 3.2 \AA corre-

sponding to $\sigma_{\text{inst}} \simeq 60 \text{ km s}^{-1}$ at $H\alpha$. All the galaxy and stellar spectra were corrected for CCD misalignment. The sky contribution was determined by interpolating along the outermost $10''\text{--}30''$ at the two edges of the slit, where the galaxy or stellar light was negligible, and then subtracted. A sky subtraction better than 1% was achieved. Each spectrum was flux-calibrated using the sensitivity function obtained from the flux standard star spectrum of the corresponding night. In each run the spectra obtained for the same galaxy along the same axis were coadded using the center of the stellar continuum as a reference, thus improving the signal-to-noise ratio (S/N) of the final two-dimensional spectrum. The spectra of the template stars were deredshifted to laboratory wavelengths.

4.2. Stellar Kinematics

The stellar kinematics of the galaxies was measured from the galaxy absorption features present in the wavelength range and centered on the Mg I line triplet ($\lambda\lambda 5164, 5173, 5184$) using the Penalized Pixel-Fitting (pPXF; Cappellari & Emsellem 2004) and Gas and Absorption Line Fitting (GANDALF; Sarzi et al. 2006) IDL⁹ codes adapted for dealing with MDM spectra.

The spectra of runs 1 and 2 were rebinned along the dispersion direction to a logarithmic scale, and along the spatial direction to obtain an $S/N \geq 40$ per resolution element. It decreases to $S/N \approx 20$ per resolution element at the outermost radii. The quality of the final spectrum depends on the resulting S/N. Examples of central spectra obtained in runs 1 and 2 covering the quality classes listed in Table 2 are shown in Figure 3. The quality parameter is 1 for $S/N \geq 100$ per resolution element, 2 for $50 \leq S/N < 100$, and 3 for $30 \leq S/N < 50$.

At each radius a linear combination of template stellar spectra from the empirical library by Sánchez-Blázquez et al. (2006, i.e., the MILES library) was convolved with the line-of-sight velocity distribution (LOSVD) and fitted to the observed galaxy spectrum by χ^2 minimization in pixel space. The LOSVD was assumed to be a Gaussian plus third- and fourth-order Gauss-Hermite polynomials \mathcal{H}_3 and \mathcal{H}_4 , which describe the asymmetric and symmetric deviations of the LOSVD from a pure Gaussian profile (van der Marel & Franx 1993; Gerhard 1993). This allowed us to derive profiles of the line-of-sight velocity (v), velocity dispersion (σ), and third- (H_3) and fourth-order (H_4) Gauss-Hermite moments of the stars.

The galaxy spectra were convolved with a Gaussian function to match the MILES spectral resolution (FWHM = 2.5 \AA ; Beifiori et al. 2010). Bad pixels coming from imperfect subtraction of cosmic rays and sky emission lines were properly masked and excluded from the fitting procedure. Ionized-gas emission lines were simultaneously fitted and a fourth-order additive Legendre polynomial was added to correct for the different shape of the continuum in the galaxy and template spectra.

The uncertainties for the kinematic parameters were estimated by Monte Carlo simulations. The simulated spectra were obtained by convolving the template spectra with an LOSVD parameterized as a Gauss-Hermite series and adding photon, readout, and sky noise. The simulated spectra were measured as if they were real. Extensive testing was performed to provide an estimate of the biases of the pPXF method with the adopted instrumental setup and spectral sampling. No bias was found in the ranges of S/N and σ which characterize the spectra of the sample galaxies. The values of H_3 and H_4 measured for the

⁹ The Interactive Data Language is distributed by ITT Visual Information Solutions.

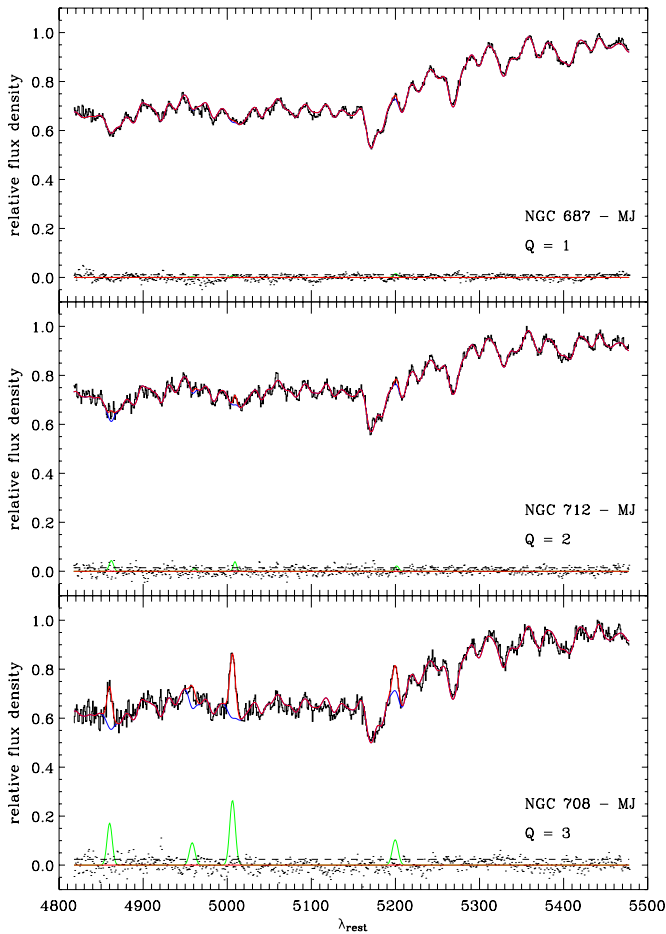


Figure 3. Example of central spectra covering the range of quality classes of runs 1 and 2. Relative fluxes have false zero points for viewing convenience. In each panel the best-fitting model (red line) is the sum of the spectra of the ionized-gas (green line) and stellar component (blue line). The latter is obtained convolving the synthetic templates with the best-fitting LOSVD and multiplying them by the best-fitting Legendre polynomials. The residuals (dots) are obtained by subtracting the model from the spectrum. The dashed line corresponds to the rms of the residuals.

(A color version of this figure is available in the online journal.)

simulated spectra differ from the intrinsic ones only within the measured errors.

The measured stellar kinematics are reported in Table 6 where velocities are relative to the galaxy centers. The folded kinematic profiles are plotted in Figure 4. The multiple observations of IC 171, NGC 679, and UGC 1308 agree within the errors.

Figure 5 shows the comparison between the measurements of σ obtained along the major axis of the sample galaxies and values available in the literature. The mean difference in velocity dispersion with respect to the measurements by Wegner et al. (1999) is $\langle \Delta \log \sigma \rangle = 0.0008 \pm 0.0054$ and has a scatter $\sigma_{\Delta \log \sigma} = 0.023$. The central velocity dispersion of all the sample galaxies, except for NGC 712 and UGC 1308, was measured by Bernardi et al. (2002) and Wegner et al. (2003) too. The mean difference is $\langle \Delta \log \sigma \rangle = -0.012 \pm 0.013$ with $\sigma_{\Delta \log \sigma} = 0.032$. Our values thus agree with published data sets within their measured errors.

Figure 6 shows the central values of σ obtained along the minor and diagonal axes of the sample galaxies as a variance-weighted mean of the values available within an aperture of $3''$. They are plotted as a function of the corresponding values obtained along the major axis. Most of the data are consistent

within 3σ errors. No systematic effects are observed for the remaining ones.

4.3. Ionized-gas Kinematics

The ionized-gas kinematics were measured from the emission lines present in the spectra of run 3, namely [N II] $\lambda\lambda 6548, 6583$, H α , [S II] $\lambda\lambda 6716, 6731$. Each observed emission line was fitted by a Gaussian, while describing the stellar continuum with a low-order polynomial. The Gaussians were assumed to share the same line-of-sight velocity (v_{gas}) and velocity dispersion (σ_{gas}). A flux ratio of 1:2.96 was assumed for the [N II] doublet, as dictated by atomic physics (e.g., Osterbrock 1989).

The best-fitting Gaussian parameters were derived using a nonlinear least-squares minimization based on the robust Levenberg–Marquardt method by Moré et al. (1980). The actual computation has been done using the MPFIT algorithm (Markwardt 2009) under the IDL environment. We averaged adjacent spectral rows to increase the S/N of the relevant emission lines. All the spectra of run 3 have $S/N < 30$ per resolution element in the continuum and were assigned to quality class 4 (Table 2). We checked that the error in the kinematic parameter determination derived by Monte Carlo simulations did not differ significantly from the formal errors given as output by the least-squares fitting routine. We therefore decided to assume the latter as error bars on the gas kinematics.

The measured ionized-gas kinematics are reported in Table 7 where velocities are given relative to galaxy centers and velocity dispersions are corrected for instrumental FWHM. The folded kinematic profiles are plotted in Figure 4.

4.4. Line-strength Indices

The Mg, Fe, and H β line-strength indices were measured following Faber et al. (1985) and Worthey et al. (1994) from flux calibrated spectra obtained in runs 1 and 2. The average iron index $\langle \text{Fe} \rangle = (\text{Fe}_{5270} + \text{Fe}_{5335})/2$ (Gorgas et al. 1990) and the combined magnesium–iron index with $[\text{MgFe}] = (\text{Mgb}(\text{Fe}))^{1/2}$ (González 1993) were computed too. Spectra were rebinned in the dispersion direction as well as in the radial direction as before. The difference between our spectral resolution and that of the Lick/IDS system (FWHM = 8.6 \AA ; Worthey & Ottaviani 1997) was taken into account by degrading our spectra to match the Lick/IDS resolution before measuring the line-strength indices. The original Lick/IDS spectra are not flux-calibrated contrary to ours. Such a difference in the continuum shape is expected to introduce small systematic offsets of the measured values of the indices. To establish these offsets and to calibrate our measurements to the Lick/IDS system, the values of the line-strength indices measured for the templates were compared to those obtained by Worthey et al. (1994). Figure 7 shows the differences between our and Lick/IDS line-strength indices for the stars observed in runs 1 and 2. The offsets were evaluated as the mean of the differences between our and Lick/IDS line-strength values, and neglected if they were smaller than the mean error of the differences. The latter was the case for H β , Mg $_2$, and Mg b for which no offset was adopted. On the contrary, it was applied as an offset to the measured values of Fe $_{5270}$ ($\Delta \text{Fe}_{5270} = -0.29 \text{ \AA}$ for run 1, -0.28 \AA for run 2) and Fe $_{5335}$ ($\Delta \text{Fe}_{5335} = -0.48 \text{ \AA}$ for run 1, -0.44 \AA for run 2) to bring our data to the Lick/IDS system. No focus correction was applied because atmospheric seeing was the dominant effect during observations (see Mehlert et al. 1998 for details). Errors on indices were derived from photon statistics and CCD readout noise, and calibrated by means of Monte Carlo simulations.

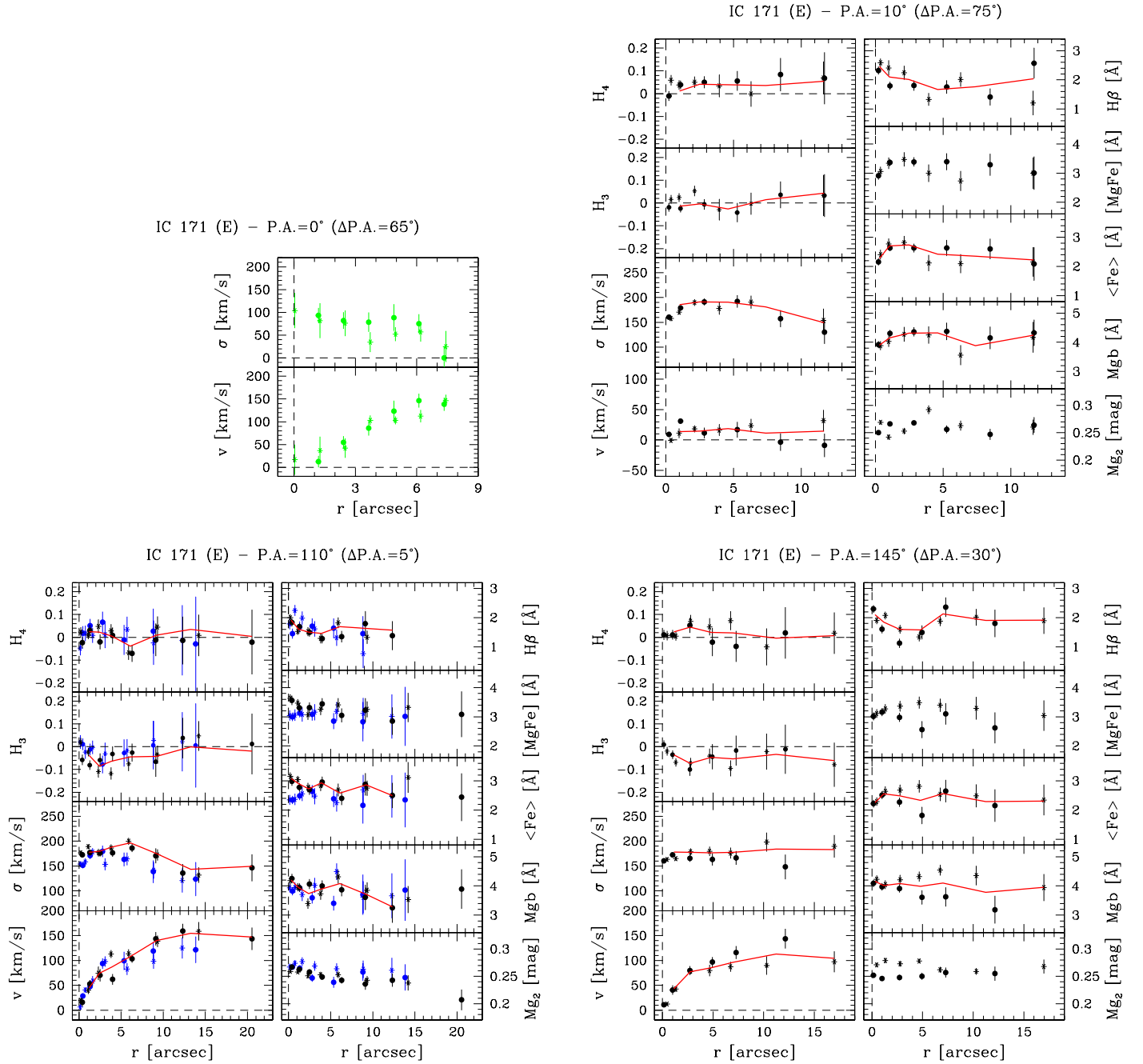


Figure 4. Kinematic parameters of the stars (run 1: black symbols; run 2: blue symbols) and ionized gas (run 3: green symbols) and the line-strength indices measured along the observed axes of the sample galaxies. For each axis the curves are folded around the nucleus. Circles and asterisks (or squares) refer to data measured along the receding and approaching side, respectively. The radial profiles of the line-of-sight velocity (v) after the subtraction of systemic velocity, velocity dispersion (σ), third-, and fourth-order coefficient of the Gauss-Hermite decomposition of the LOSVD (H_3 and H_4) are shown in the left panels (from top to bottom). The red solid lines correspond to the stellar kinematic parameters of the best-fitting dynamical model. The difference between the position angle of the observed axis and that adopted in the dynamical model for the galaxy line of nodes (Table 4) is given in the top label ($\Delta P.A.$). The radial profiles of the line-strength indices $H\beta$, $[MgFe]$, $\langle Fe \rangle$, Mgb , and Mg_2 are plotted in the right panels (from top to bottom). The red solid lines correspond to the line-strength indices derived from SSP models. (An extended version of this figure is available in the online journal.)

The measured values of $H\beta$, $[MgFe]$, $\langle Fe \rangle$, Mgb , and Mg_2 are listed in Table 8 and plotted in Figure 4. Figure 6 shows the central values of $H\beta$, $[MgFe]$, $\langle Fe \rangle$, Mgb , and Mg_2 obtained along the minor and diagonal axes of the sample galaxies as a variance-weighted mean of the values available within an aperture of $3''$ and those obtained along the corresponding major axes. Most of the data are consistent within 3σ errors. No systematic effects are observed for the remaining ones.

4.5. Properties of the Stellar Populations

The traditional and effective method of studying stellar-population properties uses diagrams of different pairs of line-strength indices. Here, the modeling of the line-strength indices measured in the previous section followed the method described in Saglia et al. (2010) and Pu et al. (2010). Among the measured line-strength indices, $H\beta$, $\langle Fe \rangle$, and Mgb were considered since

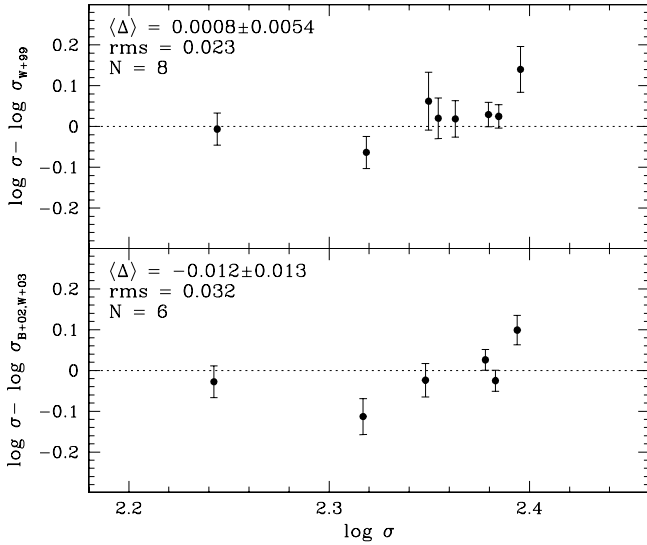


Figure 5. Central values of the stellar velocity dispersion σ measured along the major axis of the sample galaxies are compared to those available in Wegner et al. (1999, W+99), Bernardi et al. (2002, B+02), and Wegner et al. (2003, W+03).

$H\beta$ is sensitive to early-type stars and thus useful as an age indicator, $\langle Fe \rangle$ gives the metal abundance, and Mgb covers the α -element abundance. The SSP models of Maraston (1998, 2005) and the models of Lick/IDS line-strength indices with the α -element overabundance of Thomas et al. (2003) were spline interpolated on a fine grid in age t (up to 15 Gyr on steps of 0.1 Gyr), metallicity $[Z/H]$ (from -2.25 to 0.67 dex on steps of

0.02 dex) and overabundances $[\alpha/Fe]$ (from -0.3 to 0.5 dex on steps of 0.05 dex). At each radius r of the galaxies the best-fit values of τ , $[Z/H]$, and $[\alpha/Fe]$ were determined by minimizing the χ^2 function

$$\chi^2(r) = \Delta^2 H\beta(r) + \Delta^2 Mgb(r) + \Delta^2 \langle Fe \rangle(r), \quad (1)$$

where

$$\Delta^2 I(r) = \left(\frac{I(r) - I_{SSP}(\tau, [Z/H], [\alpha/Fe])}{\sigma_I(r)} \right)^2. \quad (2)$$

Here $\sigma_I(r)$ is the error on the index $I(r)$ measured at a distance r and $I_{SSP}(\tau, [Z/H], [\alpha/Fe])$ is the value predicted by the SSP models for the given set of age, metallicity, and overabundance. As in Saglia et al. (2010) and Pu et al. (2010), the best-fit values of τ , $[Z/H]$, and $[\alpha/Fe]$ are derived to the same accuracy through the χ^2 minimization by giving the same weight to $H\beta$, $\langle Fe \rangle$, and Mgb . We did not extrapolate to values outside the model grid. Therefore, the minimum χ^2 solutions are sometimes found at the edges of the parameter space. Once the set of best-fit values, i.e., the set $(\tau_{\min}, [Z/H]_{\min}, [\alpha/Fe]_{\min})$ that minimizes $\chi^2(r)$ was determined, we computed the values of the mass-to-light ratios of the corresponding SSP models for the Kroupa IMF (Y_{Kroupa}). The resulting values of Y_{Kroupa} , stellar-population ages, metallicities, and overabundances (inside r_{eff}) are given in Table 3. Errors on all quantities were derived by considering the minimal and maximal parameter variations compatible with $\Delta\chi^2 = \chi^2 - \chi^2_{\min} = 1$. Note, however, that errors on age and metallicity are correlated to some extent (Worthey 1994).

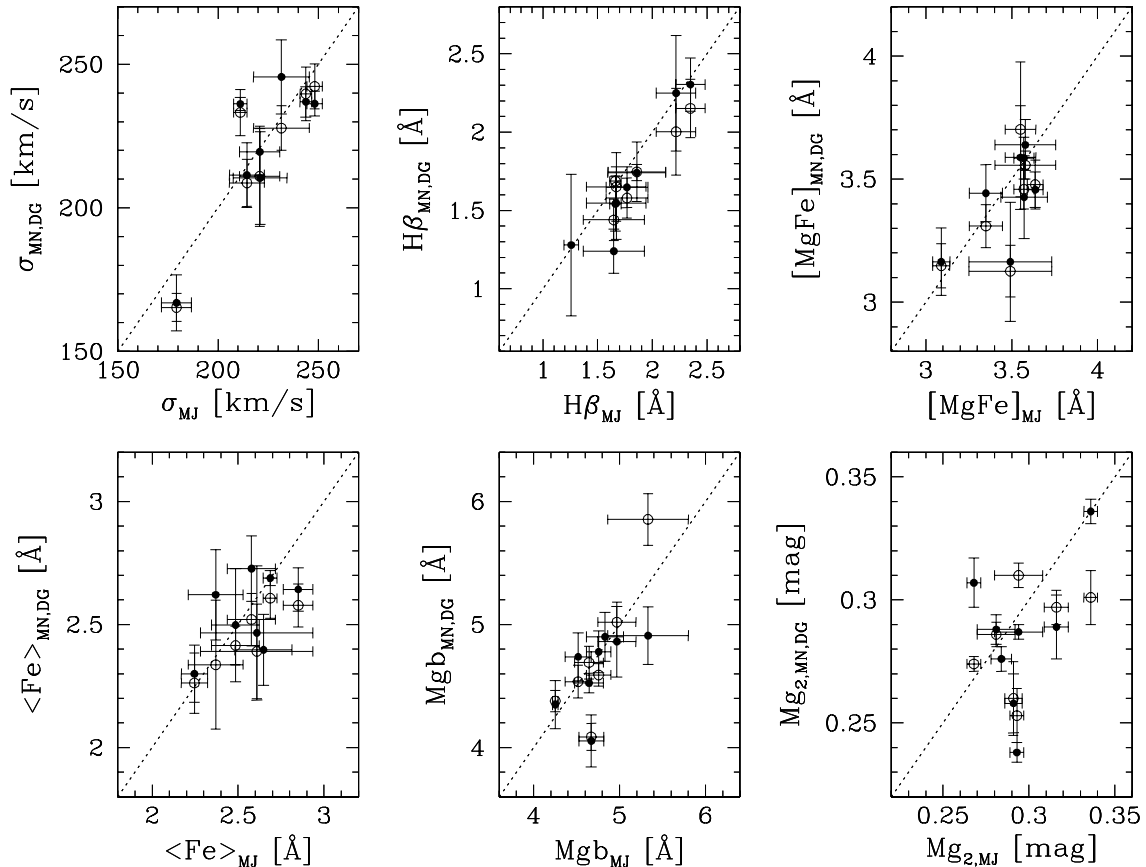


Figure 6. Central values of the stellar velocity dispersion σ and line-strength indices $H\beta$, $[MgFe]$, $\langle Fe \rangle$, Mgb , and Mg_2 measured within an aperture of $3''$ along the minor (filled circles) and diagonal axes (open circles) are compared to those measured along the major axis.

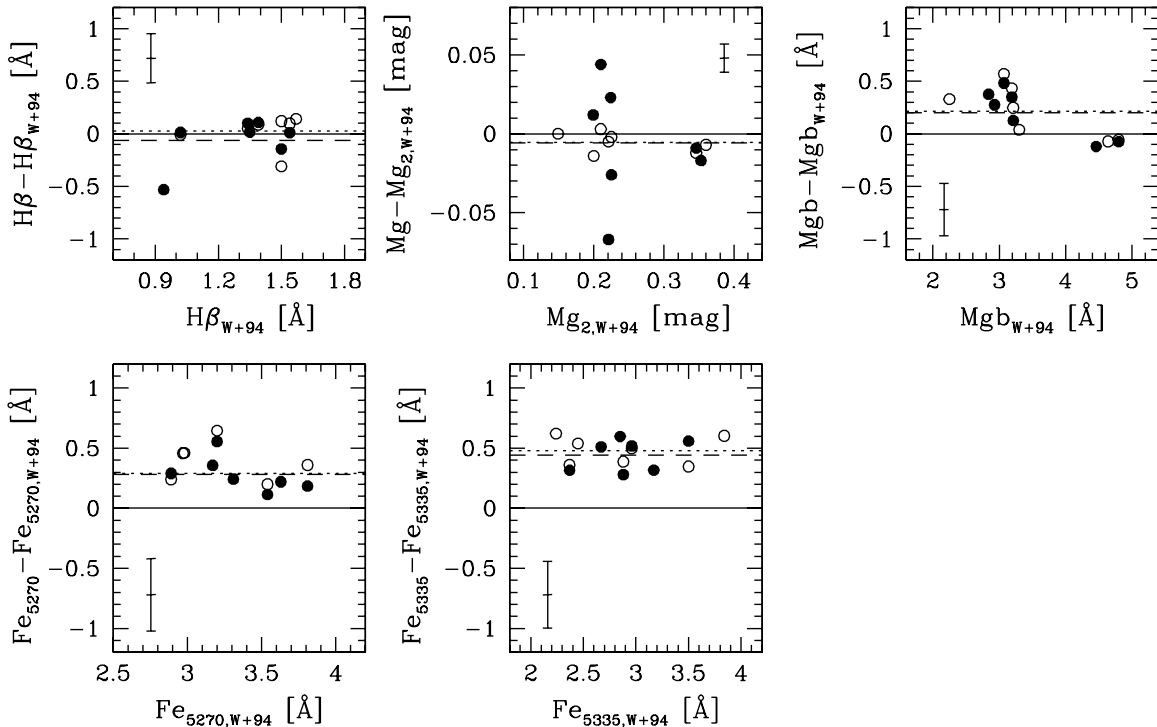


Figure 7. Comparison of the line-strength indices $H\beta$, Mg_2 , Mgb , Fe_{5270} , and Fe_{5335} measured for the stars in common with Worthey et al. (1994, W+94). In each panel the error bar in the upper left corner indicates the mean error of the difference between our values and those by Worthey et al. (1994), the continuous line shows the line of correspondence, and the dotted and dashed lines correspond to the average difference of data in run 1 (open circles) and in run 2 (filled circles), respectively.

Table 3
Stellar-population Parameters Averaged Inside r_{eff}

Object	Y_{Krou} ($M_{\odot} L_{\odot}^{-1}$)	τ (Gyr)	[Z/H]	$[\alpha/\text{Fe}]$	z_*
(1)	(2)	(3)	(4)	(5)	(6)
IC 171 (E)	3.22 ± 0.70	9.0 ± 2.4	0.12 ± 0.10	0.08 ± 0.05	$1.3^{+1.3}_{-0.6}$
NGC 679 (D)	3.65 ± 0.29	9.7 ± 1.0	0.21 ± 0.05	0.31 ± 0.02	$1.5^{+0.5}_{-0.3}$
NGC 687 (C)	3.72 ± 0.44	9.9 ± 1.6	0.17 ± 0.07	0.22 ± 0.03	$1.6^{+1.1}_{-0.5}$
NGC 703 (I)	2.15 ± 0.32	5.2 ± 1.2	0.23 ± 0.05	0.45 ± 0.02	$0.5^{+0.2}_{-0.1}$
NGC 708 (A)	4.17 ± 1.05	11.0 ± 3.1	0.19 ± 0.14	0.39 ± 0.05	$2.2^{+\infty}_{-1.2}$
NGC 712 (F)	2.42 ± 0.37	6.2 ± 1.4	0.20 ± 0.08	0.39 ± 0.03	$0.7^{+0.2}_{-0.2}$
NGC 759 (G)	2.75 ± 0.31	7.1 ± 0.9	0.16 ± 0.07	0.35 ± 0.04	$0.8^{+0.2}_{-0.1}$
UGC 1308 (B)	3.07 ± 1.06	8.8 ± 4.4	0.07 ± 0.16	0.30 ± 0.10	$1.2^{+5.0}_{-0.8}$

Notes. Column 1: Name. Column 2: SSP mass-to-light ratio Y_{Krou} in the Kron-Cousins R band. Column 3: SSP age τ . Column 4: SSP metallicity [Z/H]. Column 5: SSP α -element overabundance $[\alpha/\text{Fe}]$. Column 6: Star formation redshift z_* .

5. DYNAMICAL MODELING

As discussed in Section 1, the dynamical modeling follows our previous work as in Thomas et al. (2007a, 2007b, 2009b) and is based on the orbit superposition technique (Schwarzschild 1979) as implemented in Thomas et al. (2004, 2005b). We first determined the stellar luminosity density from the surface-brightness profile by deprojection into a three-dimensional, axisymmetric distribution with specified inclination, using the simulated annealing scheme implemented by Magorrian (1999). This algorithm reconstructs the luminosity density nonparametrically on a set of ≈ 250 sampling points in a plane perpendicular to the equatorial one and crossing the galactic center.

The adopted inclinations of the galaxies are given in Table 4. The nearly round dust features in NGC 679, NGC 759, and UGC 1308 suggest that these galaxies are almost face-on and we deprojected them at the lowest inclination compatible with a system that is intrinsically not flatter than an E7 galaxy. In all other galaxies, except NGC 687, the projected ellipticity reaches $\epsilon \approx 0.4$ at some radius and we assumed that these galaxies are edge-on ($i = 90^\circ$). The inclination of NGC 687 is unclear, but the galaxy is slightly flattened without showing any significant rotation at almost all radii and we assumed that this galaxy is edge-on too. For the galaxies where no *HST* images were available, we deprojected the ground-based surface brightness taking into account seeing convolution as in Rusli et al. (2011). The solid lines in Figure 2 show the photometric

Table 4
Mass-to-light Ratio, Parameters of the Dark Matter Halo, Stellar Velocity Dispersion,
and Geometric Parameters Adopted for the Dynamical Model

Object	Model	Υ_* ($M_\odot L_\odot^{-1}$)	f_{halo}	$\log_{10}(\rho_{\text{halo}})$ ($M_\odot \text{pc}^{-3}$)	z_{DM}	σ_{eff} (km s^{-1})	i_{stars} ($^\circ$)	P.A. _{stars} ($^\circ$)
(1)	(2)	(3)	(4)	(5)	(6)	(7)	(8)	(9)
IC 171 (E)	NFW	$3.5^{+0.5}_{-0.5}$	$0.41^{+0.18}_{-0.12}$	$-2.17^{+0.33}_{-0.14}$	0.7	211.4 ± 1.5	90	115
NGC 679 (D)	NFW	$4.0^{+0.5}_{-0.5}$	$0.27^{+0.13}_{-0.11}$	$-1.00^{+0.25}_{-0.04}$	1.3	252.7 ± 0.9	30	150
NGC 687 (C)	LOG	$3.5^{+0.5}_{-1.0}$	$0.36^{+0.21}_{-0.07}$	$-1.03^{+0.08}_{-0.21}$...	237.4 ± 1.3	90	120
NGC 703 (I)	LOG	$9.5^{+0.5}_{-0.5}$	$0.001^{+0.062}_{-0.001}$	$-3.12^{+1.56}_{-\infty}$	3.7	233.3 ± 1.2	90	45
NGC 708 (A)	SC	$7.5^{+1.0}_{-2.5}$	<0.41	<-2.11	0.8	189.2 ± 1.6	90	130
NGC 712 (F)	SC	$8.5^{+0.5}_{-0.5}$	<0.06	<-1.84	4.0	225.2 ± 0.9	90	85
NGC 759 (G)	LOG	$4.5^{+0.5}_{-0.5}$	$0.48^{+0.04}_{-0.18}$	$-1.22^{+0.17}_{-0.25}$	2.8	231.0 ± 1.1	40	20
UGC 1308 (B)	SC	$2.6^{+0.1}_{-0.1}$	<0.20	<-1.95	...	202.6 ± 1.8	50	110

Notes. Column 1: Name. Column 2: Type of best-fit mass model (LOG: logarithmic halo, NFW: NFW halo, SC: self-consistent, i.e., no dark matter halo). Column 3: Dynamical mass-to-light ratio Υ_* (including all the mass that follows the light) in the Kron-Cousins R band. Column 4: Spherically averaged halo-mass fraction within r_{eff} . Column 5: Average halo density within $2r_{\text{eff}}$. Column 6: Dark-halo assembly redshift z_{DM} . Column 7: Velocity dispersion σ_{eff} inside r_{eff} . Column 8: Assumed galaxy inclination i_{stars} . Column 9: Position angle P.A._{stars} of the line of nodes measured north through east adopted for the dynamical model.

Table 5
Photometric Parameters of the Sample Galaxies

a (arcsec)	μ_R (mag arcsec $^{-2}$)	e	P.A. ($^\circ$)	Δx_c (arcsec)	Δy_c (arcsec)	Err. ^a (arcsec)	a_3/a $\times 100$	b_3/a $\times 100$	a_4/a $\times 100$	b_4/a $\times 100$	a_6/a $\times 100$	b_6/a $\times 100$	Err. ^b
IC 171													
0.202 ± 0.000	16.927 ± 0.010	0.000 ± 0.000	90.0 ± 0.0	0.127	0.594	0.000	0.00	0.00	0.00	0.00	0.00	0.00	0.00
0.644 ± 0.081	17.005 ± 0.014	0.317 ± 0.121	66.7 ± 16.1	0.000	0.000	0.057	-2.21	3.91	2.94	-1.95	2.36	-1.64	1.25
1.104 ± 0.010	17.146 ± 0.015	0.182 ± 0.010	78.4 ± 1.9	0.024	0.006	0.007	-0.94	0.85	0.55	0.03	-0.18	-0.45	0.41
1.482 ± 0.007	17.338 ± 0.014	0.186 ± 0.006	82.3 ± 1.1	0.036	0.012	0.005	-0.67	0.85	0.27	0.06	-0.28	-0.01	0.29
1.797 ± 0.006	17.530 ± 0.012	0.170 ± 0.004	84.1 ± 0.7	0.048	0.006	0.004	-0.23	0.77	-0.07	-0.02	-0.30	-0.09	0.17
2.118 ± 0.006	17.690 ± 0.011	0.176 ± 0.003	85.9 ± 0.7	0.061	0.000	0.004	0.24	0.75	-0.21	0.07	-0.34	-0.05	0.12
2.455 ± 0.007	17.845 ± 0.012	0.186 ± 0.003	88.5 ± 0.6	0.079	-0.006	0.005	0.51	0.75	-0.23	0.13	-0.12	0.16	0.15
2.805 ± 0.009	17.993 ± 0.010	0.187 ± 0.004	91.4 ± 0.7	0.091	-0.006	0.006	-0.91	-0.49	0.14	0.18	-0.07	0.40	0.19
3.240 ± 0.012	18.149 ± 0.009	0.205 ± 0.004	95.4 ± 0.7	0.109	-0.006	0.009	-0.96	0.79	0.62	-0.19	0.28	0.09	0.22
3.760 ± 0.013	18.322 ± 0.008	0.222 ± 0.004	98.1 ± 0.6	0.121	-0.024	0.009	-0.69	1.04	0.28	-0.44	0.32	-0.17	0.19

Notes.

^a Error on the center coordinates derived from the residual rms of the ellipse fit to the isophotes: $\text{Err} = \text{rms}_{\text{fit}}/\sqrt{N}$ with $N \leq 128$ the number of fitted points of the isophote.

^b Error of Fourier coefficients defined as $\text{Err} = \left(\frac{\sum_{i=10}^{N/2} (a_i^2 + b_i^2)}{N/2 - 10} \right)^{1/2} \times \frac{100}{a}$.

(This table is available in its entirety in machine-readable and Virtual Observatory (VO) forms in the online journal. A portion is shown here for guidance regarding its form and content.)

Table 6
Stellar Kinematics of the Sample Galaxies

r (arcsec)	V (km s^{-1})	σ (km s^{-1})	H_3	H_4	P.A. ($^\circ$)	Run
IC 171						
-11.71	-8.8 ± 19.3	130.4 ± 24.0	0.033 ± 0.094	0.068 ± 0.114	10	2
-8.47	-3.5 ± 14.2	157.4 ± 17.2	0.036 ± 0.059	0.084 ± 0.073	10	2
-5.27	16.9 ± 12.8	192.1 ± 12.7	-0.042 ± 0.042	0.056 ± 0.043	10	2
-2.84	11.5 ± 8.7	191.1 ± 7.2	-0.006 ± 0.023	0.050 ± 0.026	10	2
-1.08	31.1 ± 3.7	178.9 ± 4.5	-0.024 ± 0.016	0.039 ± 0.018	10	2
-0.23	9.3 ± 3.6	160.4 ± 4.1	-0.019 ± 0.018	-0.010 ± 0.021	10	2
0.38	0.6 ± 3.7	157.7 ± 5.1	-0.016 ± 0.019	0.059 ± 0.023	10	2
0.98	-11.1 ± 8.0	170.3 ± 4.9	-0.024 ± 0.019	0.038 ± 0.021	10	2
2.12	-18.3 ± 5.7	189.8 ± 6.6	-0.053 ± 0.023	0.050 ± 0.025	10	2
3.94	-16.3 ± 9.3	178.0 ± 12.1	0.029 ± 0.046	0.034 ± 0.049	10	2

(This table is available in its entirety in machine-readable and Virtual Observatory (VO) forms in the online journal. A portion is shown here for guidance regarding its form and content.)

Table 7
Ionized-gas Kinematics of the Sample Galaxies

r (arcsec)	V (km s ⁻¹)	σ (km s ⁻¹)	P.A. (°)	Run
IC 171				
-7.34	138.4 ± 14.8	0.0 ± 24.9	0	4
-6.11	146.2 ± 15.4	75.4 ± 21.0	0	4
-4.88	123.1 ± 23.5	88.6 ± 29.3	0	4
-3.65	85.8 ± 16.2	78.6 ± 21.6	0	4
-2.42	54.8 ± 13.7	82.1 ± 18.3	0	4
-1.19	12.4 ± 12.1	93.4 ± 16.0	0	4
0.04	-16.9 ± 32.8	104.0 ± 38.6	0	4
1.27	-36.9 ± 30.4	81.8 ± 38.5	0	4
2.50	-42.2 ± 21.3	76.1 ± 28.2	0	4
3.73	-103.2 ± 10.1	34.8 ± 21.4	0	4
4.96	-103.0 ± 8.8	52.3 ± 15.2	0	4
6.19	-112.3 ± 13.7	56.9 ± 21.2	0	4
7.42	-146.3 ± 12.5	24.9 ± 33.7	0	4
NGC 703				
-2.46	-125.2 ± 31.3	137.7 ± 33.5	0	4
-1.23	-75.5 ± 20.4	223.6 ± 18.1	0	4
0.00	30.0 ± 66.0	259.6 ± 53.7	0	4
1.23	90.4 ± 36.3	176.2 ± 62.0	0	4
2.46	80.2 ± 25.1	0.0 ± 114.0	0	4
NGC 708				
-4.92	-161.3 ± 18.5	125.2 ± 21.3	0	4
-3.69	-162.5 ± 6.9	116.8 ± 10.3	0	4
-2.87	-141.1 ± 3.6	120.2 ± 7.9	0	4
-1.23	-96.7 ± 3.6	144.6 ± 7.8	0	4
0.00	1.6 ± 4.3	189.8 ± 7.9	0	4
1.23	88.7 ± 2.8	146.7 ± 7.5	0	4
2.46	145.7 ± 3.3	103.6 ± 7.8	0	4
3.69	191.8 ± 2.7	85.9 ± 7.6	0	4
4.92	218.2 ± 4.0	78.9 ± 8.5	0	4
6.15	257.5 ± 5.4	78.9 ± 9.7	0	4
7.38	267.4 ± 4.3	73.6 ± 8.9	0	4
8.61	284.1 ± 12.2	89.4 ± 16.2	0	4
20.09	302.6 ± 15.1	48.0 ± 25.3	0	4
-18.86	-261.9 ± 15.2	56.8 ± 23.3	40	4
-17.22	-263.2 ± 10.5	44.0 ± 19.2	40	4
-15.99	-251.4 ± 12.0	81.0 ± 16.4	40	4
-14.76	-220.5 ± 11.1	89.7 ± 15.1	40	4
-13.53	-193.9 ± 6.3	86.2 ± 10.3	40	4
-12.30	-193.1 ± 4.2	84.4 ± 8.6	40	4
-11.07	-183.7 ± 3.9	87.8 ± 8.3	40	4
-9.84	-180.7 ± 4.0	91.3 ± 8.4	40	4
-8.61	-169.5 ± 4.1	88.0 ± 8.4	40	4
-7.38	-152.6 ± 3.5	70.5 ± 8.2	40	4
-6.15	-158.5 ± 3.3	81.9 ± 8.0	40	4
-4.92	-158.1 ± 4.2	91.1 ± 8.5	40	4
-3.69	-126.7 ± 6.9	129.3 ± 10.2	40	4
-2.46	-79.8 ± 5.9	135.7 ± 9.3	40	4
-1.23	-45.8 ± 3.8	160.2 ± 7.8	40	4
0.00	0.0 ± 2.7	172.1 ± 7.3	40	4
1.23	48.4 ± 4.0	156.2 ± 7.9	40	4
2.46	105.9 ± 6.5	127.6 ± 9.9	40	4
3.69	162.0 ± 8.6	114.0 ± 11.8	40	4
5.33	192.6 ± 20.3	131.9 ± 23.0	40	4
-6.77	-190.9 ± 15.6	114.4 ± 18.8	130	4
-5.54	-178.0 ± 8.0	106.8 ± 11.4	130	4
-4.31	-163.6 ± 6.9	130.5 ± 10.1	130	4
-3.08	-114.8 ± 6.4	139.5 ± 9.6	130	4
-1.85	-79.2 ± 5.1	141.4 ± 8.7	130	4
-0.62	-42.1 ± 3.9	153.8 ± 7.9	130	4
0.61	52.7 ± 3.4	177.9 ± 7.5	130	4
1.84	154.3 ± 2.9	161.8 ± 7.4	130	4
3.07	187.5 ± 4.5	119.0 ± 8.5	130	4

Table 7
(Continued)

r (arcsec)	V (km s ⁻¹)	σ (km s ⁻¹)	P.A. (°)	Run
4.30	179.0 ± 8.8	108.5 ± 12.1	130	4
5.53	177.1 ± 8.6	79.9 ± 12.8	130	4
6.76	186.6 ± 5.8	90.0 ± 9.8	130	4
7.99	194.0 ± 7.0	83.0 ± 11.1	130	4
9.22	212.8 ± 12.5	122.6 ± 15.3	130	4
14.55	290.0 ± 11.9	70.5 ± 17.2	130	4
16.60	286.6 ± 27.3	60.1 ± 39.4	130	4
NGC 712				
-5.29	-23.8 ± 21.3	76.6 ± 28.1	0	4
-2.42	-40.0 ± 12.0	98.0 ± 15.6	0	4
-1.19	-10.7 ± 41.2	154.9 ± 41.5	0	4
0.04	1.6 ± 22.8	167.5 ± 118.1	0	4
1.27	33.1 ± 40.2	106.2 ± 46.5	0	4
2.50	19.4 ± 16.9	70.7 ± 23.3	0	4
5.37	20.5 ± 30.8	28.5 ± 73.0	0	4
NGC 759				
-5.41	-152.7 ± 6.1	55.6 ± 11.3	0	4
-3.77	-163.3 ± 2.2	46.7 ± 7.8	0	4
-2.54	-153.3 ± 2.3	57.7 ± 7.6	0	4
-1.31	-112.9 ± 4.6	111.8 ± 8.6	0	4
-0.08	4.4 ± 10.8	172.2 ± 12.2	0	4
1.15	122.4 ± 4.0	104.1 ± 8.3	0	4
2.38	148.7 ± 3.7	64.4 ± 8.5	0	4
3.61	146.1 ± 2.5	51.1 ± 7.9	0	4
5.66	160.4 ± 5.3	53.9 ± 10.5	0	4
-5.45	52.3 ± 4.1	53.6 ± 9.2	100	4
-3.81	49.8 ± 2.4	58.6 ± 7.7	100	4
-2.58	48.9 ± 5.5	99.6 ± 9.4	100	4
-1.35	40.8 ± 5.4	137.8 ± 8.9	100	4
-0.12	4.8 ± 9.9	161.8 ± 11.8	100	4
1.11	-28.7 ± 6.3	127.0 ± 9.6	100	4
2.34	-49.1 ± 2.9	83.5 ± 7.7	100	4
3.57	-56.7 ± 2.8	47.1 ± 8.3	100	4
5.21	-62.1 ± 6.8	37.2 ± 14.8	100	4
-5.49	-84.4 ± 7.4	66.1 ± 12.2	145	4
-3.85	-75.5 ± 4.7	86.5 ± 8.9	145	4
-2.62	-66.6 ± 4.4	115.1 ± 8.5	145	4
-1.39	-38.1 ± 3.9	152.1 ± 7.9	145	4
-0.16	-2.2 ± 9.0	164.7 ± 11.0	145	4
1.07	57.2 ± 7.8	133.3 ± 10.8	145	4
2.30	70.3 ± 3.1	93.6 ± 7.8	145	4
3.53	73.5 ± 3.4	72.0 ± 8.2	145	4
5.17	65.9 ± 5.9	64.3 ± 10.6	145	4
UGC 1308				
-4.02	149.7 ± 46.7	66.2 ± 63.9	0	4
-1.15	143.2 ± 24.4	130.7 ± 27.1	0	4
0.08	0.0 ± 78.0	180.1 ± 73.8	0	4
1.31	-71.2 ± 41.9	87.1 ± 51.5	0	4
2.54	-74.2 ± 39.3	48.5 ± 63.4	0	4

(This table is also available in machine-readable and Virtual Observatory (VO) forms in the online journal.)

profiles obtained by projecting the deprojected stellar luminosity density.

As a second step, we modeled the total mass distribution of the galaxies as the sum of two components:

$$\rho = \rho_* + \rho_{\text{halo}}, \quad (3)$$

where ρ_* is the density of matter (either luminous or dark) that is distributed like the stars and ρ_{halo} is the density of dark

matter distributed in a halo. The mass-to-light ratio of the matter distributed like the stars is

$$\Upsilon_* = \rho_*/\nu, \quad (4)$$

where ν is the deprojected stellar luminosity density. Note that ρ_* measures all the matter following the light (it may include dark matter as well as stars). In contrast, ρ_{halo} is the halo density (some of the dark matter may not follow this profile) and its distribution is assumed to be either a cored logarithmic profile (Binney & Tremaine 1987)

$$\rho_{\text{LOG}}(r) = \frac{V_c^2}{4\pi G} \frac{3r_c^2 + r^2}{(r_c^2 + r^2)^2} \quad (5)$$

or an NFW profile (Navarro et al. 1996)

$$\rho_{\text{NFW}}(r) \propto \frac{1}{r(r+r_s)^2}, \quad (6)$$

implemented as in Thomas et al. (2007b). In either case the halo is assumed to be spherical. Cored logarithmic halos have an asymptotically constant circular velocity V_c and a flat density core inside $r < r_c$.

Then, the gravitational potential Φ was computed by integrating Poisson's equation. Thousands of orbits were calculated in this fixed potential. The orbits were superposed to fit the observed LOSVDs following the luminosity density constraint. The maximum entropy technique of Richstone & Tremaine (1988) was used to fit the kinematic data. The maximum entropy technique is a method for modeling galaxies from limited observations. While many distribution functions are consistent with the collisionless Boltzmann equation and the observational data, statistical mechanics and information theory suggest that the most natural ones have the largest entropy. The function

$$\hat{S} = S - \alpha \chi^2 \quad (7)$$

is maximized, where S is an approximation to the Boltzmann entropy and χ^2 is the sum of the squared residuals to the kinematic data. The smoothing parameter α controls the influence of the entropy S on the orbital weights. Thomas et al. (2005b) used Monte Carlo simulations to derive the optimal α for a typical long-slit setup.

The best-fit dark-halo densities, dark-halo mass fractions, and mass-to-light ratios Υ_* of the mass that is tied to the light are given in Table 4. The corresponding best-fitting lines to the kinematic data are shown in Figure 4.

6. COMPARISON WITH STRONG GRAVITATIONAL LENSES AND KINEMATICS OF THE IONIZED GAS

The statistical significance and accuracy of the methods employed here have been previously tested. Thomas et al. (2005b) checked the axisymmetric orbit superposition code with mock observations of Coma galaxies and used Monte Carlo simulations to show that internal velocity moments could be reconstructed to $\approx 15\%$. In Thomas et al. (2007b), the mass-to-light ratio, halo-mass fraction, and shape of the circular velocity curve from the dynamical modeling of 17 Coma early-type galaxies are shown to be robust against the choice of the regularization parameter α .

A more severe modeling uncertainty is the unknown flattening of the galaxies along the line of sight. Even if all galaxies were

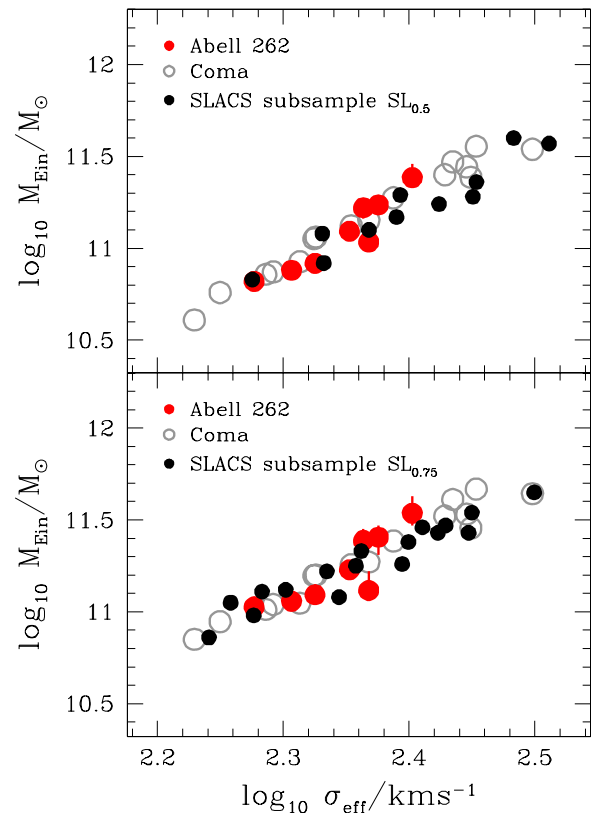


Figure 8. Projected total mass, M_{Ein} , within a fiducial Einstein radius, r_{Ein} , as a function of the effective velocity dispersion, σ_{eff} , for the galaxies in A262 (red filled circles; the error bars are smaller than the symbols in most cases), the Coma Cluster (open circles; Thomas et al. 2011), and the SLACS survey (Auger et al. 2009; black filled circles). The dynamical masses from two-component models with dark halos ($\rho = \Upsilon_* \times \nu + \rho_{\text{halo}}$) are shown. The lensing galaxies are divided into the $\text{SL}_{0.5}$ (with $\langle r_{\text{Ein}}/r_{\text{eff}} \rangle \approx 0.5$, top panel) and $\text{SL}_{0.75}$ (with $\langle r_{\text{Ein}}/r_{\text{eff}} \rangle \approx 0.75$, bottom panel) subsamples, respectively.

(A color version of this figure is available in the online journal.)

perfectly axisymmetric, their flattening along the line of sight is not directly observable and can only be inferred from the apparent flattening if the inclination is given. For early-type galaxies this is in general not the case and, moreover, even with the help of stellar kinematics the inclination remains only weakly constrained (e.g., Krajnović et al. 2005; van den Bosch & van de Ven 2009). However, dynamical mass-to-light ratios turn out to be robust against the inclination mismatch (e.g., Krajnović et al. 2005; Thomas et al. 2005b; van den Bosch & van de Ven 2009). The dynamical masses can be biased by up to a factor of two only if the flattening along the line of sight is significantly underestimated (as in the case of an almost face-on disk modeled as a spheroid) (Thomas et al. 2007a). In addition, the mass recovery in the axisymmetric approximation becomes dependent on viewing angle and shape for significantly triaxial galaxies. End-on views of prolate/triaxial models give 20%–30% overestimated masses, while for highly flattened face-on systems masses are underestimated by up to 50% (Thomas et al. 2007a).

Both published masses of gravitationally strong lenses that are structurally similar to our galaxies and our limited emission-line data for the galaxies in A262 provide valuable checks on our foregoing analysis.

6.1. Comparison with Strong Gravitational Lensing

Figure 8 compares the projected dynamical masses of the A262 galaxies with strong gravitational lenses from SLACS

Table 8
Line-strength Indices of the Sample Galaxies

r (arcsec)	H β (\AA)	[MgFe] (\AA)	$\langle\text{Fe}\rangle$ (\AA)	Mgb (\AA)	Mg ₂ (mag)	P.A. ($^\circ$)	Run
IC 171							
-11.71	2.571 ± 0.518	3.004 ± 0.562	2.086 ± 0.566	4.326 ± 0.445	0.264 ± 0.014	10	2
-8.47	1.410 ± 0.294	3.287 ± 0.376	2.603 ± 0.352	4.151 ± 0.388	0.247 ± 0.010	10	2
-5.27	1.754 ± 0.223	3.394 ± 0.281	2.635 ± 0.263	4.371 ± 0.289	0.256 ± 0.007	10	2
-2.84	1.804 ± 0.176	3.386 ± 0.157	2.632 ± 0.149	4.357 ± 0.159	0.268 ± 0.004	10	2
-1.08	1.792 ± 0.145	3.367 ± 0.119	2.634 ± 0.111	4.303 ± 0.123	0.266 ± 0.003	10	2
-0.23	2.322 ± 0.136	2.908 ± 0.130	2.157 ± 0.126	3.920 ± 0.122	0.250 ± 0.003	10	2
0.38	2.585 ± 0.148	3.056 ± 0.168	2.404 ± 0.167	3.884 ± 0.157	0.269 ± 0.004	10	2
0.98	2.409 ± 0.259	3.342 ± 0.196	2.770 ± 0.195	4.031 ± 0.191	0.242 ± 0.005	10	2
2.12	2.241 ± 0.242	3.471 ± 0.244	2.819 ± 0.230	4.273 ± 0.253	0.253 ± 0.006	10	2
3.94	1.329 ± 0.216	3.000 ± 0.301	2.117 ± 0.277	4.249 ± 0.297	0.292 ± 0.008	10	2

(This table is available in its entirety in machine-readable and Virtual Observatory (VO) forms in the online journal. A portion is shown here for guidance regarding its form and content.)

(Auger et al. 2009). The comparison is done exactly as in Thomas et al. (2011) and we refer the reader to this paper for further details. We find no significant differences between the A262 galaxies, Coma galaxies, and SLACS lenses, respectively. Note that the scatter in the dynamical masses is not larger than in the lensing masses. This implies that possible biases in the dynamical modeling related to spatially limited kinematic observations and/or symmetry assumptions are unlikely (as they would increase the scatter in dynamical masses of galaxies observed at random viewing angles). That the Coma and A262 galaxies must have nearly axisymmetric shapes is consistent with the lack of isophotal twists or minor-axis rotation in the photometric and kinematic observations, respectively (except for IC 171 and NGC 708; cf. Section 6.2).

6.2. Comparison between Circular Velocity and Ionized-gas Rotation Velocity

Figure 10 compares the circular velocity v_{circ} obtained from stellar dynamics and rotation velocity v_{rot} of the ionized gas. The comparison is restricted to radii r_{gas} where the pressure support in the gas component is small ($\sigma_{\text{gas}} \leq 60 \text{ km s}^{-1}$) and therefore the gas velocity is supposed to trace v_{circ} (Bertola et al. 1995; Pignatelli et al. 2001; Dalcanton & Stilp 2010). The line-of-sight gas velocity v_{gas} is derived from the observed one after subtracting the systemic velocity and folding around the galaxy center. It was deprojected into v_{rot} by assuming that the gaseous component rotates in circular orbits in an infinitesimally thin disk. The orientation of the gaseous disk with respect to the line of sight is given by its inclination (i_{gas}) and the P.A. of its line of nodes (P.A._{gas}). Therefore, it is

$$v_{\text{rot}} = \frac{v_{\text{gas}}}{\sin i_{\text{gas}} \cos \vartheta}, \quad (8)$$

where

$$\vartheta = \arctan \frac{\tan \Delta \text{P.A.}_{\text{gas}}}{\cos i_{\text{gas}}} \quad (9)$$

and

$$\Delta \text{P.A.}_{\text{gas}} = \text{P.A.}_{\text{gas}} - \text{P.A.}_{\text{slit}}. \quad (10)$$

$\text{P.A.}_{\text{slit}}$ is the position angle of the slit where v_{gas} is measured. Likewise, the deprojected radius is

$$r = r_{\text{gas}} \cos \vartheta \cos \Delta \text{P.A.}_{\text{gas}}. \quad (11)$$

In an axisymmetric spheroidal system, the position angle $\text{P.A.}_{\text{stars}}$ of the stellar isophotes is constant with radius and a rotating gaseous disk is confined to the equatorial plane. Hence, the unique stellar $\text{P.A.}_{\text{stars}}$ coincides with the P.A._{gas} of the gaseous disk. The same holds for the inclinations. For the ionized-gas component of the A262 galaxies we only have observations along a few slits and can neither verify the assumption of an infinitesimally thin disk nor, given the case, derive its orientation (i.e., P.A._{gas} and i_{gas}) directly. Therefore, we performed two different deprojections of the gas kinematics for each galaxy.

First, we assumed that the galaxy is an axisymmetric spheroid and deprojected the gas kinematics with $i_{\text{gas}} = i_{\text{stars}}$ and $\text{P.A.}_{\text{gas}} = \text{P.A.}_{\text{stars}}$ from the dynamical model (Table 4). The corresponding values v_{rot} are open dots in Figure 10 (when missing, they fall outside the plot range). We used $i_{\text{gas}} = 85^\circ$ when the dynamical model has $i_{\text{stars}} = 90^\circ$ since an infinitesimally thin and exactly edge-on gas disk would not be observable at any P.A. different from the galaxy's major axis.

Second, since the isophotal P.A. of the A262 galaxies shows some scatter, we varied i_{gas} and P.A._{gas} and minimized the χ^2 -difference between v_{rot} and v_{circ} . The P.A._{gas} was changed between the minimum and maximum values measured for the P.A. of the galaxy isophotes. The best-fitting values of v_{rot} are shown by the filled circles in Figure 10. For each galaxy, the figure also quotes i_{gas} and P.A._{gas} for both sets of deprojection. IC 171 was treated separately, as discussed below.

As Figure 10 shows, using the same P.A. and i for both the gaseous disks and dynamical models did not yield good agreement between v_{rot} and v_{circ} . However, varying i_{gas} and P.A._{gas} allowed matching the gas kinematics with predictions of the dynamical models quite well. The corresponding inclinations i_{gas} differ from the i_{stars} values of the dynamical models by less than 10° . The inclination of an elliptical galaxy can, at best, be derived dynamically with an uncertainty of $\pm 20^\circ$ (e.g., Krajnović et al. 2005; Thomas et al. 2005b; van den Bosch & van de Ven 2009). Thus, a $\Delta i \leq 10^\circ$ is well within the uncertainties of the dynamical models.

The case for the P.A.s is more complicated. To ease the comparison with the orientation of the stars in the galaxies, the P.A. panels in Figure 2 show the P.A.s adopted in the two deprojection sets. The red solid line corresponds to $\text{P.A.}_{\text{gas}} = \text{P.A.}_{\text{stars}}$ and gives the open circles for v_{rot} plotted

in Figure 10. The gray solid line marks the gas orientation that minimizes the χ^2 between gas rotation and dynamical v_{circ} and leads to the filled circles for v_{rot} given in Figure 10. The dotted lines in Figure 2 delimit the 68% confidence region of P.A._{gas} .

The ionized-gas kinematics for our A262 galaxies has limited spatial coverage and radial extension because only a few slits were observed. Nevertheless, this gives a valuable consistency check. Within the above limitations and when $\sigma_{\text{gas}} \leq 60 \text{ km s}^{-1}$, the gas rotation velocity is consistent with the circular velocity obtained from our axisymmetric dynamical models and supports to the total mass distributions we derived. This holds also for IC 171 and NGC 708, which are not exactly axisymmetric systems.

6.3. Notes on Individual Galaxies

In the following we discuss the A262 galaxies individually, except for NGC 679 and NGC 687, which show no detectable emission line.

IC 171. The observed isophotal twist (Figure 2) suggests that IC 171 is not exactly axisymmetric, similar to NGC 708. Moreover, v_{rot} do not match the dynamical v_{circ} for any P.A. within the observed range. If IC 171 is triaxial, the gas might also be rotating around the long axis of the galaxy. To test this geometric configuration, we tried a variety of different P.A._{gas} tilted by about 90° with respect to the photometric major axis, fixing the inclination at $i_{\text{gas}} = 85^\circ$. A $\text{P.A.}_{\text{gas}} = 13^\circ$ brings v_{rot} in agreement with v_{circ} . If the gas rotates around the long axis of the galaxy, then the line of nodes of the gaseous disk is at $\text{P.A.} = 103^\circ$. This value is consistent with the orientation of the galaxy isophotes at the corresponding deprojected radii ($r \gtrsim 3 \text{ kpc}$, Figure 2).

NGC 703. The isophotes show little variation in P.A. over all the observed radii ($30^\circ \lesssim \text{P.A.} \lesssim 50^\circ$, Figure 2). We found $\text{P.A.}_{\text{stars}} \approx \text{P.A.}_{\text{gas}}$ and $i_{\text{stars}} \approx i_{\text{gas}}$ within the scatter of the data after minimizing the χ^2 difference between dynamical circular velocity and gas rotation velocity (Figure 10). The photometric and kinematic data are consistent with our assumptions about both the stellar and gaseous components.

NGC 708. The inner and outer isophotes ($r \lesssim 2.5 \text{ kpc}$) have different orientations (Figure 2). The dynamical model was adjusted toward the galaxy center, where the stellar kinematics were measured (Figure 4) and the largest stellar rotation is at $\text{P.A.} = 130^\circ$. It vanishes at $\text{P.A.} = 40^\circ$, indicating that the P.A. of the galaxy's line of nodes is close to the $\text{P.A.}_{\text{stars}} = 130^\circ$ adopted for the dynamical model. The gas rotation differs as it is large along all the observed slits (Figure 4) and the derived P.A._{gas} is close to the P.A. measured for the outer isophotes and v_{rot} best matches v_{circ} for a nearly edge-on gas disk with $\text{P.A.}_{\text{gas}} = 34^\circ$. For $i_{\text{gas}} = 80^\circ$ the deprojected radii ($r \approx 7 \text{ kpc}$; Figure 10) fall into the region where the stellar system has a photometric $\text{P.A.} \approx 40^\circ$ (Figure 2). The twist of the isophotes indicates that the system cannot be exactly axisymmetric. However, as P.A._{gas} is consistent with the stellar orientation at the corresponding radii we infer that NGC 708 is probably only mildly triaxial and that its dynamical mass is reliable.

NGC 712. The emission-line spectrum was taken close to the galaxy minor-axis, making deprojection of v_{gas} highly uncertain. The measured rotation velocities are low (Figure 4) and, therefore, consistent with a gaseous disk with the same $i_{\text{gas}} = i_{\text{stars}}$ and $\text{P.A.}_{\text{gas}} = \text{P.A.}_{\text{stars}}$ as adopted in the dynamical model of the galaxy.

NGC 759. The P.A. of the isophotes of NGC 759 ranges between about 10° and 50° beyond radii of 0.1 kpc (Figure 2). The gas kinematics was measured along three different axes and has a regular and symmetric rotation curve and velocity dispersion profile (Figure 4). We found $\text{P.A.}_{\text{stars}} \approx \text{P.A.}_{\text{gas}}$ and $i_{\text{stars}} \approx i_{\text{gas}}$ (Figure 10) confirming the orientation and intrinsic shape obtained from the stellar dynamics.

UGC 1308. The orientation of the isophotes scatters significantly within 2 kpc , but it is constant at larger radii. For the dynamical model we adopted $\text{P.A.}_{\text{stars}} = 110^\circ$, which is representative of the orientation of the major axis of the isophotes at $r \gtrsim 2 \text{ kpc}$ (Figure 2). A much smaller $\text{P.A.}_{\text{gas}} = 47^\circ$ is needed to match v_{rot} measured along a diagonal axis with v_{circ} from stellar dynamics. However, the uncertainties in P.A._{gas} are large and the predictions of the dynamical model are formally consistent with the gas rotation. Also the measured photometric P.A. has large uncertainties because the galaxy is pretty round ($\epsilon \lesssim 0.2$; Figure 2).

7. RESULTS

In this section we discuss the results from the dynamical and stellar-population models.

7.1. Evidence for Halo Mass Not Associated with the Light

Figure 9 shows the χ^2 of Equation (7) against the dynamical mass-to-light ratios Y_* for the A262 galaxies. Three parameter fits including a logarithmic dark halo component $\rho_{\text{halo}} = \rho_{\text{LOG}}$ (Equation (5); the three parameters are Y_* , r_c , and V_c) are displayed by solid lines and we marginalized over the halo parameters. Similarly, NFW halos are shown by the dashed lines and the dotted curves are for models in which all the mass follows the light ($\rho_{\text{halo}} \equiv 0$).

The kinematics of NGC 679, NGC 687, and NGC 759 cannot be fit without $\rho_{\text{halo}} > 0$. The statistical significance is at least 3σ and the dark halos dominate beyond $r \approx 1.7 r_{\text{eff}}$, $1.4 r_{\text{eff}}$, and $1.0 r_{\text{eff}}$, respectively (Figure 10). These radii are only slightly larger than the radius r_{max} of the farthest kinematic data point. For IC 171 evidence for $\rho_{\text{halo}} > 0$ is about 2σ and the dark halo outweighs the mass following the light beyond $r \approx 2.9 r_{\text{eff}}$, which is significantly on the far side of r_{max} . For the remaining objects (NGC 703, NGC 708, NGC 712, and UGC 1308) a second mass-component ρ_{halo} does not improve the fit significantly. In fact, the best-fitting models of NGC 708, NGC 712, and UGC 1308 are obtained without any dark matter in a halo with a different mass distribution than the stars, while the best-fit halo-mass fraction inside r_{eff} in NGC 703 is $f_{\text{halo}} = 0.001$, its upper limit $f_{\text{halo}} \leq 0.06$.

In the Coma galaxy sample of Thomas et al. (2007b) the statistical significance for dark halos is over 95% for 8 (out of 17) galaxies and the halo mass takes over the mass that follows the light roughly between r_{eff} and $2 r_{\text{eff}}$. IC 171, NGC 679, NGC 687, and NGC 759 have comparable dark halos. In Coma, however, we found only one galaxy with $f_{\text{halo}} \approx 0$ (GMP 1990; Thomas et al. 2007b), whereas the A262 sample reveals four (out of eight) galaxies of this kind.

Evidence for a dark component aside from mass that follows light is not directly connected to the spatial extent of the kinematic data (indicated by the dashed horizontal lines in Figure 10). For example, the presence of halo mass in NGC 759 is highly significant, even though $r_{\text{max}} < r_{\text{eff}}$. By contrast, our measurements reach $r_{\text{max}} \approx 1.5 r_{\text{eff}}$ in NGC 712 yet the mass distribution follows the light almost exactly. Likewise, in the

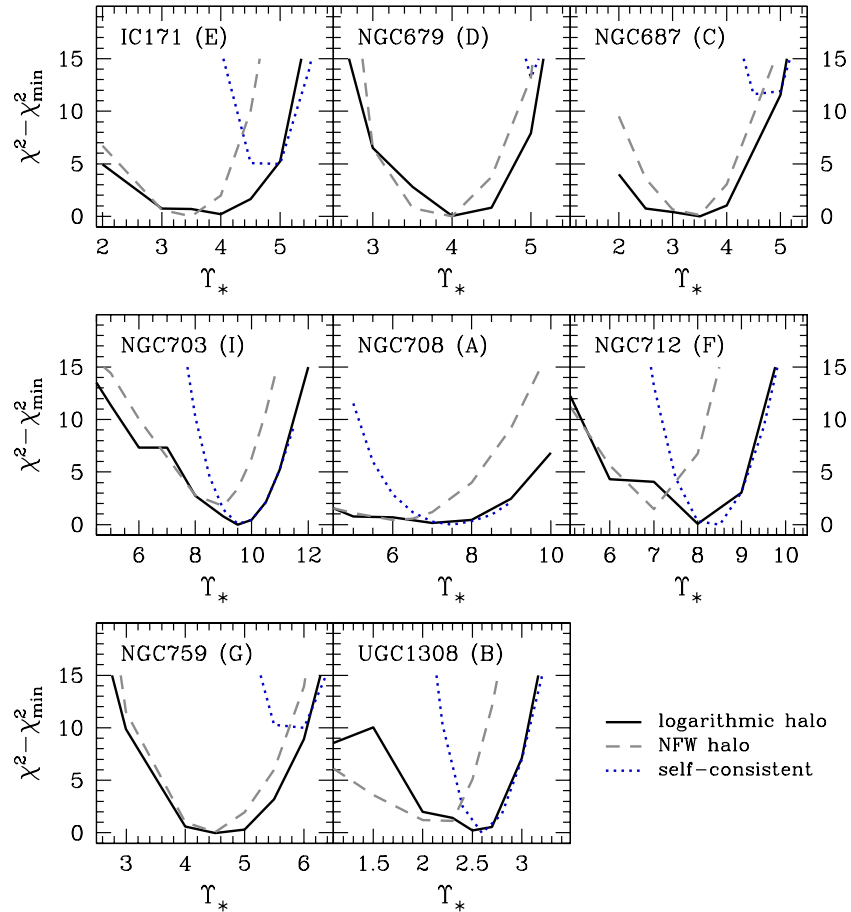


Figure 9. Goodness of the kinematic fit χ^2 (cf. Equation (7)) vs. mass-to-light ratio Υ_* . Black solid lines are for fits including a logarithmic dark matter halo; gray and dashed lines are for NFW fits; the blue and dotted lines show models where all the mass follows the light ($\rho_{\text{halo}} \equiv 0$ in Equation (3)). For each galaxy the value χ_{\min}^2 of the corresponding best-fit model is subtracted.

(A color version of this figure is available in the online journal.)

Coma galaxy GMP 1990 mass follows light out to $r_{\text{max}} \approx 3 r_{\text{eff}}$. The kinematic evidence for extra mass beyond the light is also not coupled to the degree of rotation or flattening. For example, UGC 1308 is round and shows almost no rotation, whereas NGC 712 is a moderately flattened, strong rotator and the Coma galaxy GMP 1990 is a highly flattened ($\epsilon_{\text{max}} \approx 0.6$) fast rotating system as well.

As already noted for the Coma galaxies, we cannot discriminate between NFW halos and logarithmic halos based on the quality of the kinematic fits. There is only one A262 galaxy where NFW halos fit worse by $\Delta\chi^2 \approx 2$ (NGC 703); in all other galaxies the difference is $\Delta\chi^2 \leq 1$.

7.2. Mass that Follows the Light

The two upper panels of Figure 11 plot Υ_* and the corresponding SSP Υ_{Krou} values as a function of σ_{eff} , i.e., the velocity dispersion averaged within r_{eff} . The galaxies of A262 follow trends very similar to the galaxies in the Coma Cluster. While the dynamically determined Υ_* increases strongly with σ_{eff} , the SSP models result in almost constant Υ_{Krou} . This implies that the ratio $\Upsilon_*/\Upsilon_{\text{Krou}}$ increases with σ_{eff} , as shown explicitly in the bottom panel of Figure 11.

Around $\sigma_{\text{eff}} \approx 200 \text{ km s}^{-1}$ the distribution of $\Upsilon_*/\Upsilon_{\text{Krou}}$ has a sharp cutoff with almost no galaxy below $\Upsilon_*/\Upsilon_{\text{Krou}} = 1$

(Figure 11, bottom panel). For $\sigma_{\text{eff}} \gtrsim 250 \text{ km s}^{-1}$ the lower bound of $\Upsilon_*/\Upsilon_{\text{Krou}}$ increases to $\Upsilon_*/\Upsilon_{\text{Krou}} \gtrsim 2$ at $\sigma_{\text{eff}} \approx 300 \text{ km s}^{-1}$. Similar trends are also observed in the SAURON sample (Cappellari et al. 2006; cf. the triangles in the bottom panel of Figure 11), in SLACS galaxies (Treu et al. 2010; squares in Figure 11) and, recently, in the ATLAS3d survey (Cappellari et al. 2012).

7.3. Dark Halo Densities

Figure 12 displays the average dark halo densities ($\langle \rho_{\text{halo}} \rangle$) inside $2 r_{\text{eff}}$ of Coma and A262 galaxies against the dynamical mass that follows the light $M_* = \Upsilon_* \times L$. In contrast to the Coma galaxies not all the A262 galaxies have denser dark halos than spirals. For the three A262 galaxies closest to the spiral galaxy scaling relations (NGC 703, NGC 708, and UGC 1308) we can only determine upper limits for the amount of mass that is distributed unlike the light. In these cases, models without a halo fit the data equally well within the uncertainties, or even better than models with a halo.

Still, the majority of cluster early types has 2–10 times denser halos than local spirals, implying a 1.3–2.2 times higher $(1+z_{\text{DM}})$ (assuming $\langle \rho_{\text{DM}} \rangle \sim (1+z_{\text{DM}})^3$). Thus, if spirals typically formed at $z \approx 1$, then cluster ellipticals assembled at $z_{\text{DM}} \approx 1.6$ –3.4.

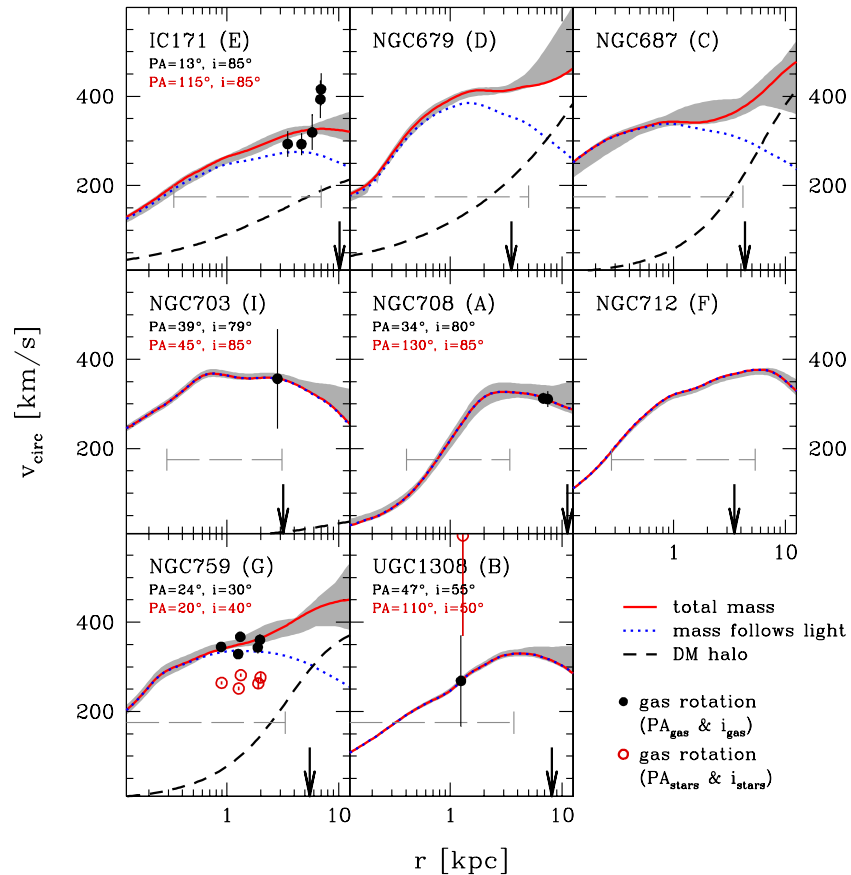


Figure 10. Rotation curves of the A262 galaxies derived from dynamical modeling. Blue dotted lines show the contribution of the mass following the light; black dashed lines are for dark halos; red solid lines give the total mass (with the 68% confidence region in gray). Long-dashed lines delimit the region with kinematic observations and the effective radius r_{eff} of each galaxy is marked by an arrow. Where detectable, we also show gas rotation measurements: red open circles correspond to the deprojected gas velocities assuming for the gaseous disk orientation the values of $P.A._{\text{stars}}$ and i_{stars} adopted for dynamical models (Table 4); black filled circles are obtained by varying $P.A._{\text{gas}}$ and i_{gas} of the gaseous disk to match the gas velocity to the circular velocity predicted by dynamical models. The best-fit $P.A._{\text{gas}}$ and i_{gas} are given. The central regions with significant pressure support ($\sigma_{\text{gas}} > 60 \text{ km s}^{-1}$) are omitted. (A color version of this figure is available in the online journal.)

7.4. Dark Matter Fractions

Averaging over all A262 galaxies we find that a fraction of $\langle f_{\text{halo}} \rangle = 0.19$ of the total mass inside r_{eff} is in a dark halo distinct from the light. The mean over the Coma galaxies is $\langle f_{\text{halo}} \rangle = 0.23$ and similar fractions come from other dynamical studies employing spherical models (e.g., Gerhard et al. 2001; Tortora et al. 2009). The A262 and Coma samples indicate an anti-correlation between $\Upsilon_*/\Upsilon_{\text{Krou}}^*$ and $\langle f_{\text{halo}} \rangle$. Galaxies where the dynamical mass following the light exceeds the Kroupa value by far ($\Upsilon_*/\Upsilon_{\text{Krou}}^* > 3$) seem to lack matter following the halo distribution inside r_{eff} ($\langle f_{\text{halo}} \rangle = 0.004$). This is not so in galaxies near the Kroupa limit ($\Upsilon_*/\Upsilon_{\text{Krou}}^* < 1.4$), where the dark-halo mass fraction is at its maximum ($\langle f_{\text{halo}} \rangle = 0.30$). The remaining galaxies are intermediate in both their $\Upsilon_*/\Upsilon_{\text{Krou}}^*$ and their halo-mass fractions ($\langle f_{\text{halo}} \rangle = 0.22$). We will return to this anti-correlation in Section 8.1.

8. DISCUSSION

Figure 11 provides strong evidence for large central mass-to-light ratios Υ_* in many early-type galaxies—especially in those with large velocity dispersions σ_{eff} . However, in all gravity-based methods there is a fundamental degeneracy concerning the interpretation of mass-to-light ratios. Such methods cannot uniquely discriminate between luminous and dark matter once

they follow similar radial distributions. The distinction is always based on the assumption that the mass-density profile of the dark matter differs from that of the luminous matter. Thus, if dark matter in massive ellipticals follows the light closer than what can be resolved by kinematic and/or lensing observations, then the dynamical mass associated with the light might not be stars only.

In fact, if the actual stellar mass-to-light ratio of a galaxy is Υ_{stars} then the stellar mass density is

$$\rho_{\text{stars}} \equiv \Upsilon_{\text{stars}} \times \nu, \quad (12)$$

while the remaining mass that follows the light,

$$\rho_{\text{DM},*} = (\Upsilon_* - \Upsilon_{\text{stars}}) \times \nu, \quad (13)$$

is a component of dark matter that follows the light—at least so closely that it is captured by Υ_* rather than the nominal ρ_{halo} . Rigorously speaking, any $0 \leq \Upsilon_{\text{stars}} \leq \Upsilon_*$ is equally consistent with the observational data and the dynamically derived dark matter distributions are correspondingly uncertain. In the following we will discuss the issue in detail.

8.1. Maximum Stellar Mass and Variable Initial Mass Function

One extreme point of view is the assumption that the stellar masses in early-type galaxies are maximal, i.e., $\Upsilon_{\text{stars}} = \Upsilon_*$

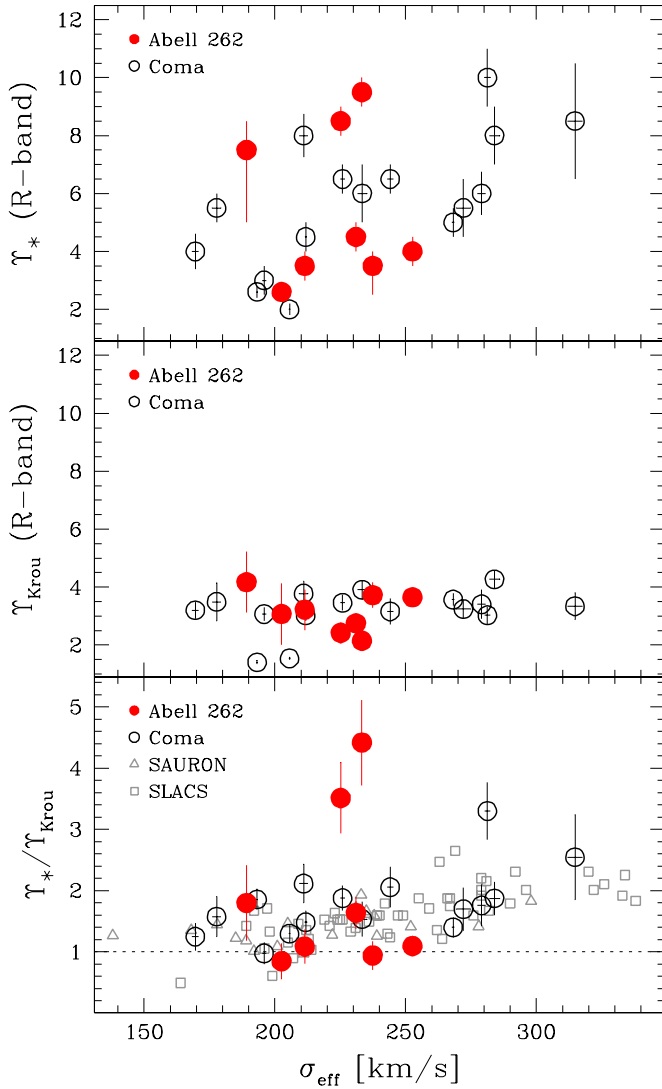


Figure 11. Dynamical Υ_* (upper panel), stellar-population Υ_{Krou} (middle panel), and the ratio $\Upsilon_*/\Upsilon_{\text{Krou}}$ (bottom panel) as a function of the effective velocity dispersion, σ_{eff} , for galaxies in A262 (filled circles) and the Coma Cluster (open circles; Thomas et al. 2011). In the bottom panel, the results for the A262 and Coma galaxies are also compared to SLACS galaxies with combined dynamical and lensing analysis (open squares; Treu et al. 2010) and SAURON galaxies with dynamical models lacking a separate dark halo (open triangles; Cappellari et al. 2006).

(A color version of this figure is available in the online journal.)

(in analogy to the maximum-disk interpretation of spiral galaxy rotation curves; e.g., van Albada & Sancisi 1986). The immediate consequence is that the stellar IMF in early-type galaxies is not universal. While around $\sigma_{\text{eff}} \approx 200 \text{ km s}^{-1}$ there are some galaxies with $\Upsilon_* \approx \Upsilon_{\text{Krou}}$ such galaxies are lacking at higher dispersions σ_{eff} (Figure 11). Recent attempts to try and measure the stellar IMF directly from near-infrared observations point in the same direction (van Dokkum & Conroy 2010, 2011; Conroy & van Dokkum 2012). These spectroscopically derived IMFs (Salpeter or steeper around $\sigma_{\text{eff}} \approx 300 \text{ km s}^{-1}$) correspond to $\Upsilon_*/\Upsilon_{\text{Krou}} \approx 1.6$ or larger (consistent with Figure 11) favoring the maximum stellar mass interpretation and an IMF varying from Kroupa-like at low velocity dispersions to Salpeter (or steeper) in the most massive early types.

As already noted for the Coma galaxies (Thomas et al. 2011), we do not see any correlation of $\Upsilon_*/\Upsilon_{\text{Krou}}$ and the SSP

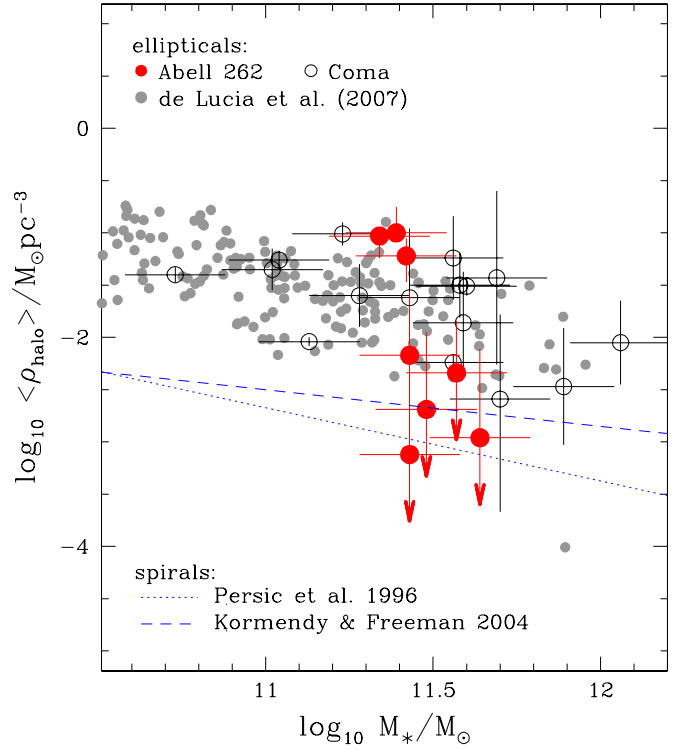


Figure 12. Average dark halo density from dynamical modeling, $\langle \rho_{\text{halo}} \rangle$, inside two effective radii as a function of the mass that follows light, M_* , for the galaxies in A262 (red filled circles) and Coma Cluster (open circles; Thomas et al. 2009b). The best-fitting halo densities among all models with a dark halo are plotted. Note that in some galaxies a better fit to the data was achieved without a separate halo component. Predictions from semi-analytic galaxy formation models (De Lucia & Blaizot 2007) are indicated by the gray filled circles. The lines show spiral galaxy scaling relations from two different studies (blue dotted line: Persic et al. 1996a, 1996b; blue dashed line: Kormendy & Freeman 2004). (A color version of this figure is available in the online journal.)

ages, metallicities, and α -element overabundances of the A262 galaxies. Such correlations could be expected if the IMF is variable, since a change in the relative number of low- and high-mass stars has some influence on the chemical evolution of the galaxies (e.g., Graves & Faber 2010). However, the stellar IMF acts on the metallicities and element abundances simultaneously with other variable conditions such as the depth of the potential well and star formation timescale. Hence, the lack of significant stellar-population differences between galaxies with high $\Upsilon_*/\Upsilon_{\text{Krou}}$ on the one hand and galaxies with low $\Upsilon_*/\Upsilon_{\text{Krou}}$ on the other is inconclusive with respect to the IMF.

An intriguing observation is the fact that the galaxies with the highest $\Upsilon_*/\Upsilon_{\text{Krou}}$ in the A262 and Coma Clusters ($\Upsilon_*/\Upsilon_{\text{Krou}} > 3$) have the lowest dark matter fractions ($\langle f_{\text{halo}} \rangle \approx 0$). In contrast, galaxies with $\Upsilon_*/\Upsilon_{\text{Krou}} < 1.4$ have the highest dark matter fractions ($\langle f_{\text{halo}} \rangle = 0.30$). Such an anti-correlation between $\Upsilon_*/\Upsilon_{\text{Krou}}$ and f_{halo} can easily be understood if the occasionally large Υ_* in some galaxies results from their dark matter density following the light so closely that it becomes indistinguishable from the stellar mass (at least in the inner parts at $r \lesssim r_{\text{eff}}$ considered here). The more that the actual dark matter of a galaxy leaks into the mass component of our models that follow the light, the less it is expected to reside in its nominal halo component ρ_{halo} , resulting in the observed anti-correlation between f_{halo} (measuring only the dark matter in the halo) and $\Upsilon_*/\Upsilon_{\text{Krou}}$ (also including the dark matter following the light).

We are not aware of an immediate physical explanation why a more “massive” IMF should occur in galaxies with less dark matter.

8.2. Cold Dark Matter and Halo Contraction

One option to further constrain the mass decomposition of gravity-based models is to incorporate predictions from cosmological simulations that confine the maximum amount of dark matter that can be plausibly attached to a galaxy of a given stellar mass. Napolitano et al. (2010) found that the velocity dispersions of a large sample of low-redshift early-type galaxies require high central mass-to-light ratios for the stars (consistent with a Salpeter IMF on average) when using such cosmological halos without baryon contraction. Adiabatic contraction (Blumenthal et al. 1986), instead, is able to increase the amount of dark matter in the centers of ellipticals and to lower the required stellar masses toward a Kroupa IMF (see also Napolitano et al. 2011). The recent study of Cappellari et al. (2012), using the halo-contraction scenario of Gnedin et al. (2004, 2011), finds that the IMF varies systematically with mass in early-type galaxies, which points against halo contraction to be sufficient to lower the central stellar masses. Lensing studies go in the same direction (Auger et al. 2010) and numerical simulations generally indicate that the classic adiabatic scenario overpredicts the actual contraction of dark matter halos (e.g., Gnedin et al. 2004).

Therefore, while halo contraction could in principle reconcile the observed central dynamical masses with a “light” stellar IMF, the required amount of dark matter contraction seems to be rather strong. However, this constraint against a “light” IMF is not purely empirical and we here briefly discuss the halo assembly redshifts of the A262 and Coma galaxies that result in the context of a Kroupa IMF and adiabatic contraction.

An immediate consequence of a universal Kroupa IMF is that some of the mass that follows the light is actually dark matter and needs to be combined with ρ_{halo} , i.e.,

$$\rho_{\text{DM,Krou}} = \rho_{\text{halo}} + (\Upsilon_* - \Upsilon_{\text{Krou}}) \times \nu. \quad (14)$$

The effect is to increase the dark matter fractions by about a factor of two; for example it is $\langle f_{\text{DM,Krou}} \rangle = 0.47$ in the A262 sample and the same within errors in the Coma Cluster (Thomas et al. 2011). Dark matter fractions of $\approx 50\%$ or more are generally found and required in the context of the assumption of a “light” IMF (e.g., Napolitano et al. 2010; Barnabè et al. 2011).

Based on $\rho_{\text{DM,Krou}}$ we derived the dark-halo assembly redshift z_{DM} for the A262 galaxies following Thomas et al. (2011). The basic assumption is that the (decontracted) halo density scales with the mean density of the universe at the assembly epoch, i.e., $\langle \rho_{\text{DM}} \rangle \sim (1 + z_{\text{DM}})^3$. Figure 13 compares the values of z_{DM} to the star formation redshifts z_* calculated from the stellar-population ages.

The derivation of z_{DM} involves the adiabatic decontraction of the dark matter density $\rho_{\text{DM,Krou}}$. In NGC 687 and UGC 1308, the dynamical Υ_* turns out to be lower than Υ_{Krou} , such that the dark halo to be decontracted for NGC 687 would be exactly cored logarithmic. However, the adiabatic decontraction of cored logarithmic halos is not possible (cf. Thomas et al. 2011) and NGC 687 has been omitted from the analysis. The dynamical model of UGC 1308 formally leaves no space for dark matter at all and this galaxy is also not considered in further analysis.

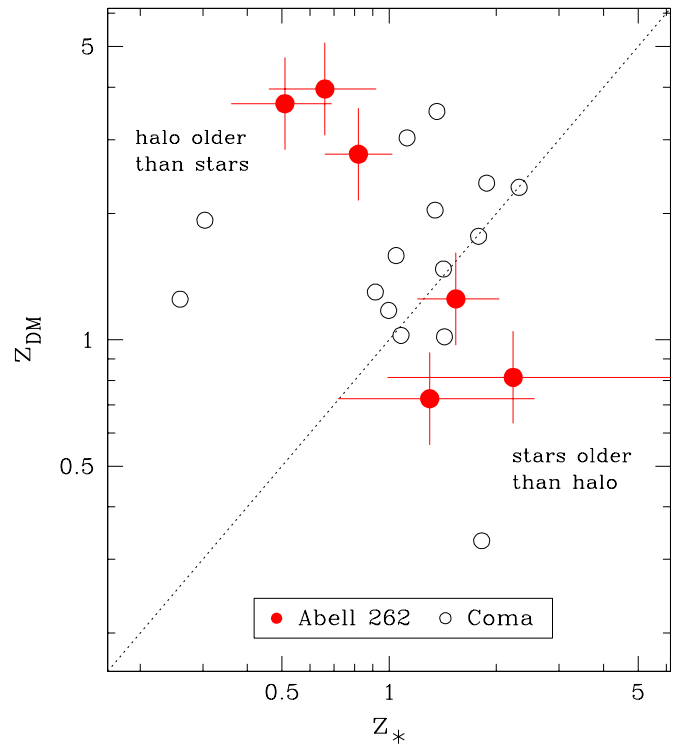


Figure 13. Kroupa-IMF-based halo assembly redshifts z_{DM} vs. star formation redshifts z_* from stellar-population ages for the galaxies in A262 (filled circles) and Coma Cluster (open circles; Thomas et al. 2011). The dotted line indicates where $z_{\text{DM}} = z_*$. The Coma galaxy GMP 5568 is in the lower right of the diagram.

(A color version of this figure is available in the online journal.)

For the A262 galaxies in Figure 13 we estimated the uncertainty in z_{DM} that comes from the scatter in the correlation between $\langle \rho_{\text{DM}} \rangle$ and $(1 + z_{\text{DM}})^3$ derived from cosmological simulations (see Figure 9 in Thomas et al. 2009b). Note that this does not include the uncertainties in ρ_{halo} or any uncertainties related to the contraction scenario. In the majority of Coma galaxies $z_{\text{DM}} \approx z_*$ and the assembly of these galaxies seems to have stopped before $z_{\text{DM}} \approx 1$. In four Coma and three A262 galaxies the stars appear younger than the halo, which indicates a secondary star formation episode after the main halo assembly.

In one Coma galaxy (GMP 5568) z_{DM} is significantly smaller than z_* . The r_{eff} of GMP 5568 is, however, about three times larger than expected for its B -band luminosity, when compared to the rest of the Coma sample. The average of its dark halo density is low because of this change in the physical scale (Thomas et al. 2011). In the A262 cluster we found two galaxies with $z_{\text{DM}} < z_*$ as well (IC 171 and NGC 708). Both galaxies have significant isophote twist (Section 6.2) and, in addition, IC 171 has boxy outskirts (Figure 2) while NGC 708 is a very slow rotator (Figure 4). The two galaxies may therefore be the remnants of gas-poor binary mergers. The virial theorem predicts the average density to drop by a factor of four during such a merger (assuming homology and equal-mass progenitors), whereas the stellar z_* remains constant (assuming similar stellar-population ages for the progenitors) due to the lack of gas available to form new stars. Thus, gasless major mergers move galaxies downward in Figure 13. In fact, the approximate decrease of the mean density to a quarter of its original value implies assembly redshifts of the hypothetical progenitors to be $z_{\text{DM}} \approx 1.7$ and $z_{\text{DM}} \approx 1.9$ for IC 171 and NGC 708, respectively. Hence, if the two galaxies have actually

recently undergone a major merger, then their progenitors may well have originated from the vicinity of the one-to-one relation in Figure 13 where we find the majority of early-type galaxies with homogeneously old stellar populations.

Without trying to overinterpret the result given the assumptions going into Figure 13 (i.e., SSP models, cosmological relations between halo density and formation redshift, and halo contraction), it seems that a universal Kroupa IMF gives a consistent picture for the formation redshifts of our galaxies.

8.3. Violent Relaxation

Apart from baryonic contraction, the central dark matter and stellar mass profiles could also become similar as a result of violent relaxation. This is usually invoked to explain the orbital structure of elliptical galaxies formed via collapse or merging (Lynden-Bell 1967; Nakamura 2000). Although many of its details are not fully understood (e.g., Arad & Lynden-Bell 2005), some general predictions can be made in the simplest cases of gas-rich (wet) and gas-poor (dry) major mergers, but it is apparent that their general evolution can be more complex. Hilz et al. (2012) further illustrate how violent relaxation in a galaxy can make the luminous and dark matter profiles similar.

In this paper, we have added data for some A262 early-type galaxies to those of our previously studied Coma galaxies. We derived the redshifts from when the stars and the dark matter halos formed and compared the profiles of the luminous and dark matter components. Some of this information could be interpreted as being consistent with signatures of violent relaxation. In particular, there are two pieces of evidence that are consistent with violent relaxation. The first is the division of the ellipticals into the two merger types as shown in Figure 13 and explained by models. Indeed recent analyses of the light distributions and dynamics of ellipticals support a picture requiring violent relaxation (Cox et al. 2006; Hopkins et al. 2009a, 2009b; Hoffman et al. 2010) with the conclusion that cuspy ellipticals grew from the mergers of gas-rich spirals while core ellipticals resulted from mergers of earlier gas-poor ellipticals with the orbital and mass distributions of the merger remnants providing a record of their progenitors (cf. Benson 2010 for a review). The second comes from Figures 10 and 11. If one makes the assumption that the stellar IMF is fixed, then the stellar and luminous matter distributions are close to being the same in several of the galaxies, which is what would be expected from violent relaxation in the merging that formed them.

Nevertheless, there are problems from some of the other galaxies. The dark matter follows the light closely in both the A262 galaxy NGC 712 and Coma galaxy GMP 1990. They are fast flattened rotators and show the least randomized orbital motions. Moreover, GMP 1990 is a highly flattened system and, taking the model results at face value, the assumption of a Kroupa IMF for this galaxy requires a highly flattened dark matter component $\rho_{\text{DM},*}$. However, as we have not tried to fit a continuous sequence of ever more flattened halos to the kinematic data, it is not clear if a model where all the mass exactly follows the light is the only way to explain the observational data. In fact, the preference for a high Y_* in the models could just reflect that the actual dark halo is flatter than the (spherical) ρ_{halo} , though still rounder than the light distribution—on a level that the data are just better approximated by increasing the mass that follows the light rather than to make the spherical component ρ_{halo} more massive. The actual flattening of the galaxy’s potential might be somewhere in

between that of the light and ρ_{halo} (spherical). Lensing galaxies do not show a significant difference between the flattening of their total mass distributions and that of their light, at least not the massive ones (Koopmans et al. 2006; Barnabè et al. 2011). If this also holds for the galaxies studied here, then either the mass that follows the light is indeed stars, or, if not, then there has to be a dark matter component that is as flattened as the stellar distribution ($\epsilon_{\text{max}} \approx 0.6$).

Admittedly, we are dealing with a small sample of imperfect observations, but at present it appears that the best one can conclude is that these data do not offer strong proof for violent relaxation being a major mechanism to make the distributions of stars and dark matter sufficiently similar.

Further numerical investigations are required to test if a predominantly collisionless accretion growth of the outer parts of massive early types can lead to a similarity of the mass-density profiles of stellar and dark matter. Simulations show that accreted stars have shallower radial mass profiles than in situ formed stars (Naab et al. 2009). Since the dark matter accretion is collisionless as well, the stellar and dark matter profiles around r_{eff} (where accreted stars are expected to dominate) might be similar.

Finally, we note that it seems unlikely that uncertainties in the modeling process (due to limited kinematic observations and/or symmetry assumptions) can explain the particularly large mass-to-light ratios of some early-type galaxies. This is mainly because our total (i.e., luminous and dark) dynamical masses are consistent with completely independent results from strong gravitational lensing and from our gas rotation velocities being consistent with the circular velocities derived from dynamical modeling.

9. SUMMARY

We presented new radially resolved spectroscopy of eight early-type galaxies in the A262 cluster. We measured the stellar rotation, velocity dispersion, and the H_3 and H_4 coefficients of the LOSVD along the major axis, minor axis, and an intermediate axis. In addition, we derived line index profiles of Mg, Fe, and $H\beta$. The ionized gas velocity and velocity dispersion were measured along different axes of six sample galaxies. Axisymmetric orbit-based dynamical models were used to derive (1) the mass-to-light ratio of all the mass that follows the light and (2) the dark halo parameters. The analysis of the ionized-gas kinematics gave a valuable consistency check for the circular velocity (and total mass distribution) predicted by dynamical modeling. Line-strength indices were analyzed by SSP models to derive the galaxies’ ages, metallicities, and α -element abundances.

This study of A262 galaxies complements our earlier work on a similar, though larger, sample of early-type galaxies in the Coma Cluster. While the Coma galaxies were selected to be mostly flattened, the A262 galaxies regarded here appear predominantly round on the sky.

Three of the new A262 galaxies show clear evidence for a mass component that is unrelated to the light with a statistical significance of at least 3σ . In one further galaxy the statistical evidence for dark matter is slightly lower (about 2σ). In four A262 galaxies the addition of mass that is distinct from the luminosity distribution does not improve the fit to the observed kinematics significantly.

We find that the dynamical mass-to-light ratios $Y_* = \rho_*/v$, where ρ_* is the density of all the mass that follows the light, increase with the stellar velocity dispersion σ_{eff} (averaged inside

r_{eff}), while the corresponding stellar-population values are almost constant. Many galaxies around $\sigma_{\text{eff}} \approx 200 \text{ km s}^{-1}$ have Υ_* consistent with a Kroupa IMF. Around $\sigma_{\text{eff}} \approx 300 \text{ km s}^{-1}$ the Υ_* are typically two times larger than for a Kroupa IMF.

This could reflect a change in the stellar IMF with σ_{eff} . However, we also find an anti-correlation between the average fraction of mass in the halo, f_{halo} , and the ratio $\Upsilon_*/\Upsilon_{\text{Kroupa}}$. The galaxies with the largest $\Upsilon_*/\Upsilon_{\text{Kroupa}}$ have the lowest halo-mass fractions inside r_{eff} and vice versa. A possible explanation for this finding is a dark matter distribution that follows the light very closely in massive galaxies and contaminates the measured Υ_* , while it is more distinct from the light in lower-mass systems.

If there is indeed some ambiguity between stellar and dark mass, then the finding of $\Upsilon_* > \Upsilon_{\text{Kroupa}}$ does not necessarily indicate a “massive” IMF. In fact, galaxies where the dynamical mass that follows the light is in excess of a Kroupa stellar population do not differ in terms of their stellar-population ages, metallicities, and α -element abundances from galaxies where this is not the case. Taken at face value, our dynamical mass models are therefore as consistent with a universal IMF as they are with a variable IMF.

However, Conroy & van Dokkum (2012) have presented stellar-population models with a variable IMF that do show a correlation with α -overabundance which can partly explain the large amount of mass that follows the light in massive early-type galaxies. Nevertheless, even these models produce stellar mass-to-light ratios that are smaller than the dynamical ones for the mass that follows the light. Therefore, a combination of both IMF variation and some degeneracy between the mass profiles of stellar and dark matter could give a consistent explanation for our observations. If the IMF indeed varies from galaxy to galaxy according to the average star formation rate, as implicated by the correlation with α -overabundance, then the assumption of a constant stellar mass-to-light ratio *inside* a galaxy should be relaxed in future dynamical and lensing models.

Finally, we have derived halo assembly redshifts for the A262 galaxies by calibrating the average dark matter density inside $2 r_{\text{eff}}$ using cosmological N -body simulations. As in Coma early types, the typical assembly redshift of the halos is around $z_{\text{DM}} \approx 1-3$.

E.M.C. acknowledges the Max-Planck-Institut für extraterrestrische Physik for hospitality while this paper was in progress. E.M.C. received support from Padua University through grants CPDA089220/08 and CPDR095001/09 and by the Italian Space Agency through grant ASI-INAF I/009/10/0. J.T. acknowledges Padua University for hospitality while this paper was in progress. Support for Program number HST-GO-10884.0-A was provided by NASA through a grant from the Space Telescope Science Institute, which is operated by the Association of Universities for Research in Astronomy, Incorporated, under NASA contract NAS5-26555. This work was supported in part by the Chinese National Science Foundation (grant No. 10821061) and the National Basic Research Program of China (grant No. 2007CB815406). We also gratefully acknowledge the Chinese Academy of Sciences and Max-Planck-Institut für Extraterrestrische Physik that partially supported this work. The authors wish to acknowledge the anonymous referee whose comments substantially improved this paper.

REFERENCES

- Abell, G. O., Corwin, H. G., Jr., & Olowin, R. P. 1989, *ApJS*, **70**, 1
- Arad, I., & Lynden-Bell, D. 2005, *MNRAS*, **361**, 385
- Auger, M. W., Treu, T., Bolton, A. S., et al. 2009, *ApJ*, **705**, 1099
- Auger, M. W., Treu, T., Gavazzi, R., et al. 2010, *ApJ*, **721**, L163
- Baggett, S., & McMaster, M. 2002, WFC2 Data Handbook, Version 4.0 (Baltimore, MD: STScI)
- Barnabè, M., Czoske, O., Koopmans, L. V. E., Treu, T., & Bolton, A. S. 2011, *MNRAS*, **415**, 2215
- Beifiori, A., Maraston, C., Thomas, D., & Johansson, J. 2010, ArXiv e-prints
- Bender, R., & Moellenhoff, C. 1987, *A&A*, **177**, 71
- Benson, A. J. 2010, *Phys. Rep.*, **495**, 33
- Bernardi, M., Alonso, M. V., da Costa, L. N., et al. 2002, *AJ*, **123**, 2990
- Bertola, F., Cinzano, P., Corsini, E. M., Rix, H.-W., & Zeilinger, W. W. 1995, *ApJ*, **448**, L13
- Binney, J., & Tremaine, S. 1987, Galactic Dynamics (Princeton, NJ: Princeton Univ. Press)
- Blanton, E. L., Sarazin, C. L., McNamara, B. R., & Clarke, T. E. 2004, *ApJ*, **612**, 817
- Blumenthal, G. R., Faber, S. M., Flores, R., & Primack, J. R. 1986, *ApJ*, **301**, 27
- Cappellari, M., Bacon, R., Bureau, M., et al. 2006, *MNRAS*, **366**, 1126
- Cappellari, M., & Emsellem, E. 2004, *PASP*, **116**, 138
- Cappellari, M., McDermid, R. M., Alatalo, K., et al. 2012, *Nature*, **484**, 485
- Clarke, T. E., Blanton, E. L., Sarazin, C. L., et al. 2009, *ApJ*, **697**, 1481
- Colless, M., Burstein, D., Davies, R. L., et al. 1999, *MNRAS*, **303**, 813
- Colless, M., Burstein, D., Wegner, G., et al. 1993, *MNRAS*, **262**, 475
- Colless, M., Saglia, R. P., Burstein, D., et al. 2001, *MNRAS*, **321**, 277
- Collobert, M., Sarzi, M., Davies, R. L., Kuntschner, H., & Colless, M. 2006, *MNRAS*, **370**, 1213
- Conroy, C., & van Dokkum, P. 2012, arXiv:1205.6473
- Corsini, E. M., Wegner, G., Saglia, R. P., et al. 2008, *ApJS*, **175**, 462
- Cox, T. J., Dutta, S. N., Di Matteo, T., et al. 2006, *ApJ*, **650**, 791
- Dalcanton, J. J., & Stilp, A. M. 2010, *ApJ*, **721**, 547
- David, L. P., Slyz, A., Jones, C., et al. 1993, *ApJ*, **412**, 479
- De Lucia, G., & Blaizot, J. 2007, *MNRAS*, **375**, 2
- De Lucia, G., Springel, V., White, S. D. M., Croton, D., & Kauffmann, G. 2006, *MNRAS*, **366**, 499
- de Vaucouleurs, G., de Vaucouleurs, A., Corwin, H. G., Jr., et al. 1991, Third Reference Catalogue of Bright Galaxies (Vol. 1–3, XII; Berlin: Springer)
- Faber, S. M., Friel, E. D., Burstein, D., & Gaskell, C. M. 1985, *ApJS*, **57**, 711
- Gavazzi, G., Boselli, A., Donati, A., Franzetti, P., & Scodreggio, M. 2003, *A&A*, **400**, 451
- Gavazzi, G., Pierini, D., Boselli, A., & Tuffs, R. 1996, *A&AS*, **120**, 489
- Gerhard, O. E. 1993, *MNRAS*, **265**, 213
- Gerhard, O., Kronawitter, A., Saglia, R. P., & Bender, R. 2001, *AJ*, **121**, 1936
- Gnedin, O. Y., Ceverino, D., Gnedin, N. Y., et al. 2011, arXiv:1108.5736
- Gnedin, O. Y., Kravtsov, A. V., Klypin, A. A., & Nagai, D. 2004, *ApJ*, **616**, 16
- González, J. J. 1993, PhD thesis, Univ. California
- Gorgas, J., Efsthathiou, G., & Aragon Salamanca, A. 1990, *MNRAS*, **245**, 217
- Graves, G. J., & Faber, S. M. 2010, *ApJ*, **717**, 803
- Hilz, M., Naab, T., Ostriker, J. P., et al. 2012, arXiv:1206.1597
- Hoffman, L., Cox, T. J., Dutta, S., & Hernquist, L. 2010, *ApJ*, **723**, 818
- Hopkins, P. F., Cox, T. J., Dutta, S. N., et al. 2009a, *ApJS*, **181**, 135
- Hopkins, P. F., Lauer, T. R., Cox, T. J., Hernquist, L., & Kormendy, J. 2009b, *ApJS*, **181**, 486
- Koopmans, L. V. E., Treu, T., Bolton, A. S., Burles, S., & Moustakas, L. A. 2006, *ApJ*, **649**, 599
- Kormendy, J., & Freeman, K. C. 2004, in IAU Symp. 220, Dark Matter in Galaxies, ed. S. Ryder, D. Pisano, M. Walker, & K. Freeman (Cambridge: Cambridge Univ. Press), 377
- Krajnović, D., Cappellari, M., Emsellem, E., McDermid, R. M., & de Zeeuw, P. T. 2005, *MNRAS*, **357**, 1113
- Kroupa, P. 2001, *MNRAS*, **322**, 231
- Lauer, T. R., Faber, S. M., Gebhardt, K., et al. 2005, *AJ*, **129**, 2138
- Lynden-Bell, D. 1967, *MNRAS*, **136**, 101
- Magorrian, J. 1999, *MNRAS*, **302**, 530
- Maraston, C. 1998, *MNRAS*, **300**, 872
- Maraston, C. 2005, *MNRAS*, **362**, 799
- Markwardt, C. B. 2009, in ASP Conf. Ser. 411, Astronomical Data Analysis Software and Systems XVIII, ed. D. A. Bohlender, D. Durand, & P. Dowler (San Francisco, CA: ASP), 251
- Martini, P., Regan, M. W., Mulchaey, J. S., & Pogge, R. W. 2003, *ApJS*, **146**, 353
- McMaster, M., & Biretta, J. 2008, WFC2 Instrument Handbook, Version 10.0 (Baltimore, MD: STScI)
- Mehlert, D., Saglia, R. P., Bender, R., & Wegner, G. 1998, *A&A*, **332**, 33
- Mehlert, D., Saglia, R. P., Bender, R., & Wegner, G. 2000, *A&AS*, **141**, 449

- Mehlert, D., Thomas, D., Saglia, R. P., Bender, R., & Wegner, G. 2003, *A&A*, **407**, 423
- Moré, J. J., Garbow, B. S., & Hillstom, K. E. 1980, User Guide for MINPACK-1 (Technical Report ANL-80-74; Argonne, IL: Argonne National Laboratory)
- Naab, T., Johansson, P. H., & Ostriker, J. P. 2009, *ApJ*, **699**, L178
- Nakamura, T. K. 2000, *ApJ*, **531**, 739
- Napolitano, N. R., Romanowsky, A. J., Capaccioli, M., et al. 2011, *MNRAS*, **411**, 2035
- Napolitano, N. R., Romanowsky, A. J., & Tortora, C. 2010, *MNRAS*, **405**, 2351
- Navarro, J. F., Frenk, C. S., & White, S. D. M. 1996, *ApJ*, **462**, 563
- Neill, J. D., Brodie, J. P., Craig, W. W., Hailey, C. J., & Misch, A. A. 2001, *ApJ*, **548**, 550
- Nelan, J. E., Smith, R. J., Hudson, M. J., et al. 2005, *ApJ*, **632**, 137
- Osterbrock, D. E. 1989, *Astrophysics of Gaseous Nebulae and Active Galactic Nuclei* (Sausalito, CA: Univ. Science Books)
- Osterbrock, D. E., Fulbright, J. P., Martel, A. R., et al. 1996, *PASP*, **108**, 277
- Paturel, G., Petit, C., Prugniel, P., et al. 2003, *A&A*, **412**, 45
- Persic, M., Salucci, P., & Stel, F. 1996a, *MNRAS*, **283**, 1102
- Persic, M., Salucci, P., & Stel, F. 1996b, *MNRAS*, **281**, 27
- Pignatelli, E., Corsini, E. M., Vega Beltrán, J. C., et al. 2001, *MNRAS*, **323**, 188
- Pu, S. B., Saglia, R. P., Fabricius, M. H., et al. 2010, *A&A*, **516**, A4
- Richstone, D. O., & Tremaine, S. 1988, *ApJ*, **327**, 82
- Rusli, S. P., Thomas, J., Erwin, P., et al. 2011, *MNRAS*, **410**, 1223
- Saglia, R. P., Bertschinger, E., Baggle, G., et al. 1997a, *ApJS*, **109**, 79
- Saglia, R. P., Burstein, D., Baggle, G., et al. 1997b, *MNRAS*, **292**, 499
- Saglia, R. P., Colless, M., Burstein, D., et al. 2001, *MNRAS*, **324**, 389
- Saglia, R. P., Fabricius, M., Bender, R., et al. 2010, *A&A*, **509**, A61
- Salpeter, E. E. 1955, *ApJ*, **121**, 161
- Sánchez-Blázquez, P., Peletier, R. F., Jiménez-Vicente, J., et al. 2006, *MNRAS*, **371**, 703
- Sarzi, M., Falcón-Barroso, J., Davies, R. L., et al. 2006, *MNRAS*, **366**, 1151
- Sato, K., Matsushita, K., & Gastaldello, F. 2009, *PASJ*, **61**, 365
- Schwarzschild, M. 1979, *ApJ*, **232**, 236
- Struble, M. F., & Rood, H. J. 1999, *ApJS*, **125**, 35
- Thomas, D., Maraston, C., & Bender, R. 2003, *MNRAS*, **339**, 897
- Thomas, D., Maraston, C., Bender, R., & Mendes de Oliveira, C. 2005a, *ApJ*, **621**, 673
- Thomas, J., Jesseit, R., Naab, T., et al. 2007a, *MNRAS*, **381**, 1672
- Thomas, J., Jesseit, R., Saglia, R. P., et al. 2009a, *MNRAS*, **393**, 641
- Thomas, J., Saglia, R. P., Bender, R., et al. 2004, *MNRAS*, **353**, 391
- Thomas, J., Saglia, R. P., Bender, R., et al. 2005b, *MNRAS*, **360**, 1355
- Thomas, J., Saglia, R. P., Bender, R., et al. 2007b, *MNRAS*, **382**, 657
- Thomas, J., Saglia, R. P., Bender, R., et al. 2009b, *ApJ*, **691**, 770
- Thomas, J., Saglia, R. P., Bender, R., et al. 2011, *MNRAS*, **415**, 545
- Tortora, C., Napolitano, N. R., Romanowsky, A. J., Capaccioli, M., & Covone, G. 2009, *MNRAS*, **396**, 1132
- Treu, T., Auger, M. W., Koopmans, L. V. E., et al. 2010, *ApJ*, **709**, 1195
- van Albada, T. S., & Sancisi, R. 1986, *Phil. Trans. R. Soc. A*, **320**, 447
- van den Bosch, R. C. E., & van de Ven, G. 2009, *MNRAS*, **398**, 1117
- van der Marel, R. P., & Franx, M. 1993, *ApJ*, **407**, 525
- van Dokkum, P. G., & Conroy, C. 2010, *Nature*, **468**, 940
- van Dokkum, P. G., & Conroy, C. 2011, *ApJ*, **735**, L13
- Wechsler, R. H., Bullock, J. S., Primack, J. R., Kravtsov, A. V., & Dekel, A. 2002, *ApJ*, **568**, 52
- Wegner, G., Bernardi, M., Willmer, C. N. A., et al. 2003, *AJ*, **126**, 2268
- Wegner, G., Colless, M., Baggle, G., et al. 1996, *ApJS*, **106**, 1
- Wegner, G., Colless, M., Saglia, R. P., et al. 1999, *MNRAS*, **305**, 259
- Wegner, G., Corsini, E. M., Saglia, R. P., et al. 2002, *A&A*, **395**, 753
- Wegner, G., & Grogin, N. A. 2008, *AJ*, **136**, 1
- Worthey, G. 1994, *ApJS*, **95**, 107
- Worthey, G., Faber, S. M., Gonzalez, J. J., & Burstein, D. 1994, *ApJS*, **94**, 687
- Worthey, G., & Ottaviani, D. L. 1997, *ApJS*, **111**, 377